Cell Biomaterials

Article

On-scalp printing of personalized electroencephalography e-tattoos

Graphical abstract

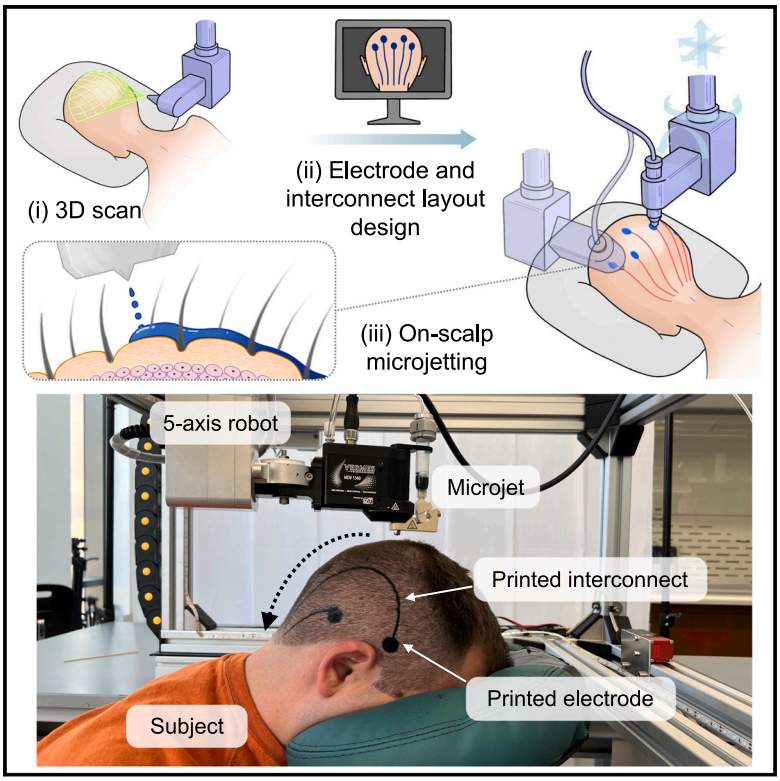

Highlights

- On-scalp-printed EEG e-tattoos offer personalized, hair-compatible brain monitoring
- Microjet printing safely, precisely, and efficiently delivers custom sensor layouts
- Electrode and interconnect inks are separately designed for sensing and conducting
- Self-drying, skin-conformable e-tattoos enable long-term, high-fidelity EEG

Authors

Luize Scalco de Vasconcelos, Yichen Yan, Pukar Maharjan, ..., José del R. Millán, Ximin He, Nanshu Lu

Correspondence

jose.millan@austin.utexas.edu (J.d.R.M.), ximinhe@ucla.edu (X.H.), nanshulu@utexas.edu (N.L.)

In brief

This study introduces a breakthrough in noninvasive brain-monitoring technology through on-scalp-printed and self-drying conductive inks for electroencephalography (EEG). These ultrathin, skin-conformable temporary e-tattoos provide a comfortable and precise way to capture brain activity, overcoming the limitations of traditional EEG systems, such as bulky equipment and manual setup. With personalized sensor layouts, distinct electrode and interconnect inks, and a hair-compatible digital printing process, these on-scalp-formed e-tattoos represent a promising tool for clinical diagnostics, brain-computer interfaces, and wearable health applications.

Scalco de Vasconcelos et al., 2025, Cell Biomaterials *1*, 100004
January 14, 2025 © 2024 Elsevier Inc. All rights are reserved, including those for text and data mining, AI training, and similar technologies.
https://doi.org/10.1016/j.celbio.2024.100004

CellPress

Cell Biomaterials

CellPress

Article

On-scalp printing of personalized electroencephalography e-tattoos

Luize Scalco de Vasconcelos,[1,9] Yichen Yan,[2,9] Pukar Maharjan,[1,8] Satyam Kumar,[3] Minsu Zhang,[3] Bowen Yao,[2] Hongbian Li,[1] Sidi Duan,[2] Eric Li,[1] Eric Williams,[1] Sandhya Tiku,[1] Pablo Vidal,[1] R. Sergio Solorzano-Vargas,[4] Wen Hong,[2] Yingjie Du,[2] Zixiao Liu,[2] Fumiaki Iwane,[3] Charles Block,[1] Andrew T. Repetski,[1] Philip Tan,[1] Pulin Wang,[1] Martín G. Martín,[4] José del R. Millán,[3,5,6,*] Ximin He,[2,*] and Nanshu Lu[1,3,6,7,8,10,*]

[1]Department of Aerospace Engineering and Engineering Mechanics, The University of Texas at Austin, Austin, TX 78712, USA
[2]Department of Materials Science and Engineering, University of California, Los Angeles, Los Angeles, CA 90095, USA
[3]Chandra Family Department of Electrical and Computer Engineering, The University of Texas at Austin, Austin, TX 78712, USA
[4]David Geffen School of Medicine, University of California, Los Angeles, Los Angeles, CA 90095, USA
[5]Department of Neurology, The University of Texas at Austin, Austin, TX 78712, USA
[6]Department of Biomedical Engineering, The University of Texas at Austin, Austin, TX 78712, USA
[7]Department of Mechanical Engineering, The University of Texas at Austin, Austin, TX 78712, USA
[8]Texas Materials Institute, The University of Texas at Austin, Austin, TX 78712, USA
[9]These authors contributed equally
[10]Lead contact
*Correspondence: jose.millan@austin.utexas.edu (J.d.R.M.), ximinhe@ucla.edu (X.H.), nanshulu@utexas.edu (N.L.)
https://doi.org/10.1016/j.celbio.2024.100004

THE BIGGER PICTURE On-scalp digital printing of custom-designed, temporary-tattoo-like sensors represents a groundbreaking advancement in noninvasive brain-monitoring technologies, advancing the fields of neuroscience, clinical diagnostics, and brain-computer interfaces (BCIs). Traditional electroencephalography (EEG) systems involve time-consuming manual electrode placement, conductive liquid gels, and cumbersome cables, which are prone to signal degradation and discomfort during prolonged use. Our approach overcomes these limitations by combining material innovations with non-contact, on-body digital printing techniques to fabricate e-tattoos that are self-drying, ultrathin, and compatible with hairy scalps. These skin-conformal EEG e-tattoo sensors enable comfortable, long-term, high-quality brain activity monitoring without the discomfort associated with traditional EEG systems. Using individual 3D head scans, custom sensor layout design, and a 5-axis microjet printing robot, we have created EEG e-tattoos with precise, tailored placement over the entire scalp. The inks for electrodes and interconnects have slightly different compositions to achieve low skin contact impedance and high bulk conductivity, respectively. After printing and self-drying, the inks form conductive, stretchable, and breathable thin films that ensure high signal fidelity, even over extended periods. This technology paves the way for non-invasive, high-performance, and user-friendly brain monitoring that will enhance both patient care and the understanding of the human brain. The broader significance of this technology lies in its potential applications beyond traditional EEG use. On-scalp printed ultrathin e-tattoos could play a pivotal role in developing BCIs for various industries, including prosthetics, virtual reality (VR), and human-robot teaming. This work also opens the possibility of on-body digital manufacture of other types of e-tattoo devices in areas beyond the head, leading to large-area, skin-covered yet deformable and breathable functional e-tattoos.

SUMMARY

Electroencephalography (EEG) is crucial for diagnosing neurological disorders and facilitating brain-computer interfaces. Traditional EEG setups with wet gels and cumbersome cables are labor intensive, uncomfortable, and degrade over time. Dry, skin-conformable e-tattoos offer a comfortable and user-friendly alternative but struggle with hairy scalps. To tackle this problem, we introduce non-contact digital printing of e-tattoos directly on the hairy scalp. Biocompatible inks are crafted for low-impedance electrodes and high-conductivity interconnects. The fabrication system includes a custom sensor layout design algorithm based on individual head scans and a 5-axis robot controlling a microjet printhead for safe and precise

All rights are reserved, including those for text and data mining, AI training, and similar technologies.

on-scalp ink delivery. After printing, these inks rapidly self-dry into conductive films perfectly conformed to scalp skin, with enhanced wearability, longevity, and skin adhesion compared with gel electrodes and transferred e-tattoos. Motion imagery and error-related potentials are effectively measured by these printed e-tattoos. This innovation heralds a new era in on-body manufacturing of personalized e-tattoos.

INTRODUCTION

Electroencephalography (EEG) is a non-invasive method that records electrical activity of the brain through sensors placed on the scalp. It has long been a diagnostic tool for conditions such as epilepsy, sleep disorders, and brain injuries as well as a popular sensing modality in neuroscience research.[1,2] Its importance has grown rapidly in recent years with the expansion of brain-computer interfaces (BCI).[3] The international 10–20 system is a widely adopted standard for electrode placement in EEG exams.[4] The "10–20" refers to the distances between the adjacent electrodes being 10% or 20% of the total distance of the skull, adjusted for individual head size. The variation of individual head shapes makes EEG caps with pre-designed openings inaccurate for electrode positioning. Therefore, in clinical settings, a well-trained EEG technician is required to manually mark electrode positions on the patient's head with a ruler and pencil, followed by gel application and cable attachment channel by channel. This laborious process is both costly and time-consuming (1∼2 h)[5] and is also susceptible to human error.[6,7] Furthermore, traditional EEG setups, with their wet-gel electrodes and dangling cables, not only pose risks of detachment and signal interference but also restrict patient mobility.[8] Over time, the gel dries and loses conductivity, limiting the measurements to less than 2 h. For long-term EEG, adhesive pastes or collodion glue are used instead but require periodic maintenance.[9,10] The discomfort caused by the cumbersome hardware can also limit patient compliance, particularly in ambulatory settings or during extended monitoring periods (see details in Note S1).

E-tattoos or epidermal electronics are ultrathin, ultrasoft, skin-conformable electronics that can perform non-invasive biometric sensing on the surface of human skin.[11,12] Traditionally, these devices are pre-fabricated on a handling substrate and subsequently transferred to the skin. However, this method struggles with hairy or highly curvilinear surfaces.[13–16] Moreover, because most biosignals are spatially distributed,[17–20] large-area sensor arrays require personalized design and accurate placement of the sensing channels to accommodate diverse user anatomy and reduce motion artifacts.[21] Although remedies for isolated issues have been reported,[22–26] a universal solution has remained unavailable.

To overcome the aforementioned challenges, we introduce digital printing of custom-designed EEG e-tattoos directly onto the hairy scalp. This approach omits the need for costly e-tattoo manufacture, tedious and inconsistent manual installation of EEG sensors, and bundles of long dangling wires (Figure 1A). It precisely places the electrodes according to the individual user's head shape. We developed printable biocompatible inks based on poly(3,4-ethylenedioxythiophene):poly(styrene sulfonate) (PEDOT:PSS), a highly promising conductive polymer material for bio-interfacing.[27–30] These low-viscosity inks are jetted through the hairs, lightly moistening the scalp before quickly self-drying into soft (Young's modulus 66 < MPa), stretchable (elongation >30%), and conductive thin films (∼ 30 μm thick) that conform perfectly to the skin microtopology without causing mechanical perception. We have formulated two distinct types of inks: one to form electrodes with low skin contact impedance to pick up the faint EEG signals from the brain and the other to form interconnects with high conductivity and high contact impedance to minimize noise pickup.

On-tissue printing is an emerging technology. Previous efforts have primarily focused on bioprinting cell-embedded hydrogels for tissue regeneration[31–33] or strain sensors,[34–36] both in very localized hairless anatomy without requiring specific ink-tissue interfacial electrical properties. Our technique is the first to produce ultrathin e-tattoos directly on human skin for electrophysiology data acquisition despite hairs. Our approach departs from previous on-tissue fabrication technologies in three major aspects (Table S1). First, personalized sensor layout design and printing over large-area, 3D-curvilinear body surfaces are automated through the combination of 3D anatomy scanning, "project-and-slice" 3D surface sensor layout design, and 5-axis robotic control (Figures 1B, 1C, and S1; Video S1). Second, non-contact, fast-speed microjet printing (Note S2; Video S2) instead of extrusion is adopted for high-speed ink droplets to reliably wet hairy skin with uniformity and continuity (Figures S2 and S3; Videos S3 and S4). Lastly, microjet-compatible PEDOT:PSS-based inks are formulated separately for ultrathin electrodes and interconnects (Figure 1D). The printed inks can fully solidify on human skin after 12 min at room temperature without any treatment (Figure 1E), rendering perfectly skin-conformed e-tattoos (Figures 1F, S4, and S5) with much higher adhesion to the skin than transferred e-tattoos (Figures 1G–1J).

RESULTS

The requirements for the inks are microjet compatibility, biocompatibility, suitable electrical and mechanical properties, and easy removal. These requirements rule out widely used ink curing methods, including UV- or thermo-induced free-radical curing; thermo-, mechanical-, or laser-sintering; or involvement of harsh chemicals. Instead, we opt for spontaneous film formation through water evaporation, as demonstrated in previous works with silver particle dispersion.[31,37–40] For user comfort and mechanical stability, the printed electrodes and interconnects should have a higher stretchability than that of human scalp skin (∼20%),[41] sufficient bending compliance,[14] good skin adhesion, good breathability, stability against sweat and oxidation, and resistance to abrasion.[42] Meanwhile, printed electrodes must have low contact impedance with the skin (40 < kΩ)[43] to achieve high noise rejection (Notes S3 and S4), which is crucial because EEG signals have an inherently low amplitude of 1–100 μV.[2] By contrast,

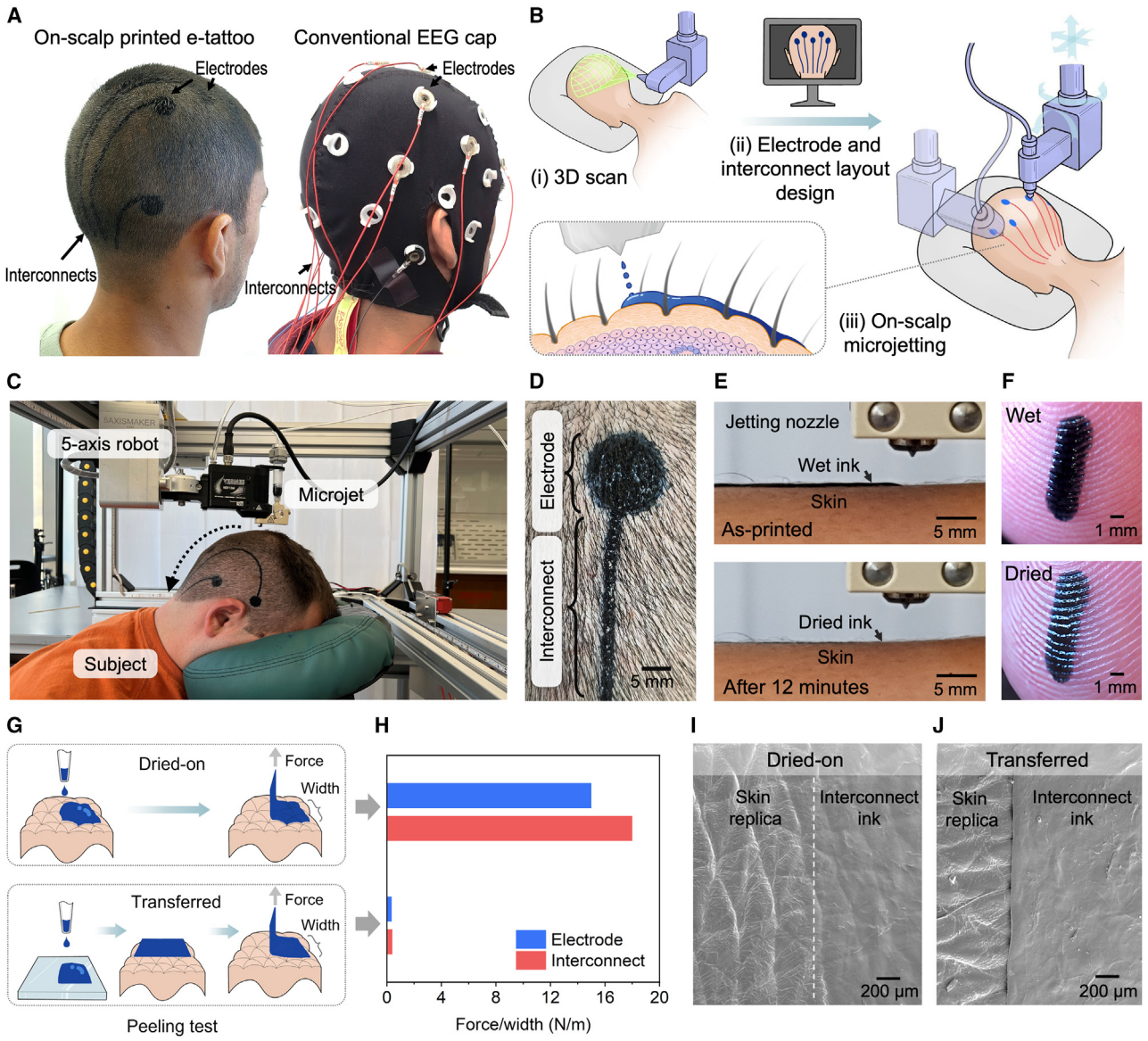

Figure 1. Overview of the on-scalp EEG e-tattoo printing technology

Figure360▷ For a Figure360 author presentation of this figure, see https://doi.org/10.1016/j.celbio.2024.100004.

(A) On-scalp printed e-tattoo (left) vs. conventional EEG cap (right).

(B) Schematic illustration of the three main steps of on-scalp e-tattoo printing: (i) 3D head scanning, (ii) personalized electrode and interconnect layout design, and (iii) on-scalp hair-compatible microjet printing.

(C) A photo of the printer setup in which a 5-axis robot controls a microjet printhead for non-contact ink dispensing.

(D) Close-up top view of an electrode and its interconnect directly printed on a hairy scalp.

(E) Close-up side view of the microjetting process on a forearm: as-jetted wet ink layer (top) and solidified thin film after 12 min (bottom).

(F) Top view of the wet ink (top) and dried ink (bottom) on a human fingertip. The solidified e-tattoo can fully conform to the fingerprints.

(G and H) Peeling tests on pig skin show that e-tattoos printed and dried on the skin exhibit much stronger adhesion than those printed on a glass substrate and subsequently transferred to the skin.

(I and J) SEM images of the e-tattoos printed on and transferred to human skin replicas. The printed e-tattoo has much better skin conformability than the transferred e-tattoo. See also Figures S1–S5 and Table S1.

printed interconnects need high skin contact impedance to avoid picking up EEG signals along the way. In addition, a low total interconnect resistance is critical for rejecting electromagnetic interference (EMI) and capacitive noise. As a result, the excessive length of the printed interconnects (up to 50 cm) has to be offset by a sufficiently high bulk conductivity (> 40 S/cm, Note S5). Therefore, two types of inks with contrasting properties need to be formed.

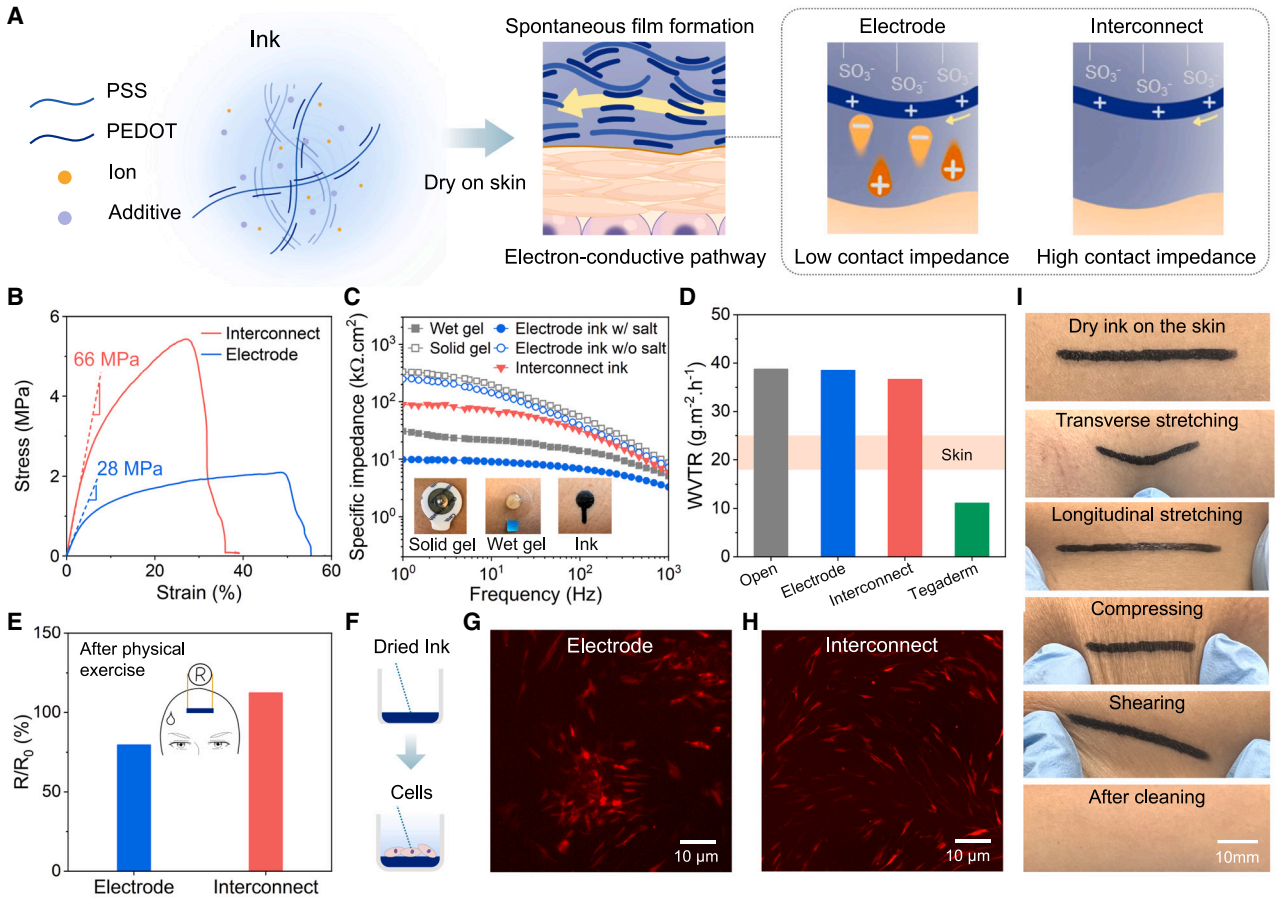

Figure 2. Properties of the on-skin-printed electrodes and interconnects

(A) Schematics of the two ink compositions tuned for distinct properties. During the ink-drying process, PEDOT will stack to form electron-conductive pathways (yellow arrow). For electrodes, ink containing NaCl promotes the low contact impedance with the skin needed for EEG acquisition. For interconnects, ink without NaCl demonstrates significantly higher contact impedance when applied to the skin, inherently inhibiting the pickup of EEG signals, whereas the addition of DMSO enhances the bulk electron conductivity required due to lengthy routing.

(B) Stress-strain curves of the dried electrode and the interconnect films show stretchability over 30%.

(C) Comparison of the specific contact impedance of different electrode inks with wet and solid commercial gel electrodes. The NaCl-containing ink has the lowest value, 9 kΩ·cm^2 at 10 Hz.

(D) Water vapor transmission rates (WVTRs) through the electrode and interconnect films are similar to that of an open vial and higher than that of the human skin.[52,53] By contrast, the 3M Tegaderm tape has a much lower WVTR.

(E) Intense physical exercises did not drastically alter the resistance of the interconnect and electrode traces.

(F) Schematic of cell culturing experiment on dried inks.

(G and H) Fluorescent images of human skin fibroblast cells grown on the electrode and interconnect films for a period of 3 days reveal favorable fiber morphologies, suggesting that both inks exhibit good biocompatibility.

(I) Photos showing that the interconnect film formed on the skin can withstand large mechanical deformations, indicating good robustness and adhesion. The interconnect can be easily removed by wiping with an alcohol wipe or soapy water, leaving no residue or discoloration on the skin. See also Figures S6–S17 and Table S2.

To meet all the aforementioned criteria using a novel approach, PEDOT:PSS (Figure 2A) was selected as the principal material for both electrode and interconnect inks because of its ability to disperse in water, form films upon drying, and its recognized biocompatibility.[44–46] Glycerol and dimethyl sulfoxide (DMSO) are also biocompatible, having been used in skincare products and as cryoprotectants in the cryopreservation of cells and biologics.[47] They were added to the interconnect ink to strike a balance between mechanical compliance and electrical conductivity. DMSO enhances both conductivity[45,48] and stretchability, but its influence maxes out at ~10% strain before breaking (Table S2). Hence, the plasticizing ability of glycerol[49,50] was used to further lower the elastic modulus to 66 MPa and enhance the stretchability to 30% (Figure 2B). Furthermore, the secondary doping effect of glycerol benefits the electrical properties,[51] resulting in a sufficiently high conductivity of 83 S/cm. Ultimately, the interconnect made from PEDOT:PSS, DMSO, and glycerol showed sufficient and stable conductivity on the skin for over 24 h of wear (Figure S6). The resistance of the free-standing interconnect thin film remained almost constant

under 100 cycles of repetitive strains between 0% and 10% (Figure S7).

For the electrode ink, sodium chloride (NaCl) was introduced to increase ionic conductivity and thus promote low contact impedance with the skin because ions can cross the stratum corneum through existing appendageal pathways.[54] Although the NaCl-free interconnect exhibited high skin contact impedance (72 kΩ. cm^2 at 10 Hz) to suppress signal pickup, the NaCl-containing electrode achieved an 8-fold lower contact impedance (9 kΩ. cm^2 at 10 Hz), which is much lower than commercial solid-gel electrodes and on par with commercial wet saline gels (Figure 2C). Note that this low contact impedance was achieved without any skin abrasion prior to ink printing (Figure S8; Note S5). The NaCl addition to the electrode ink also reduced the elastic modulus from 130 MPa (Table S2) to 28 MPa (Figure 2B), which can be attributed to the weakening of the Coulombic interactions between PEDOT and PSS.[55] Furthermore, the contact impedance remained below 40 kΩ· cm^2 for over 20 h (Figure S9) without causing any skin irritation (Figure S10), indicating its potential for long-term recording.

The tunable viscosity and shear thinning of aqueous PEDOT:PSS solutions enable excellent printability using microjetting (Figure S11; Note S2). The measured contact angles of the electrode and the interconnect inks were 47.54° and 74.52° (Figures S12A and S12B), respectively, which are in the optimal range for jet printing, allowing good adhesion and spreading on the skin while avoiding bleeding to maintain adequate printing resolution.[56] Through a covered vial setup, the water vapor transmission rate (WVTR) of the electrode and interconnect at 21.5°C and 35% humidity was measured to be 38.5 and 36.6 g · cm^{-2}· h^{-1}, respectively, which are similar to that of the control case without any cover (38.8 g · cm^{-2}· h^{-1}) (Figures 2D and S13). This high breathability can be attributed to the low thickness (∼30 μm, Figure S14) and water diffusivity of the PEDOT:PSS film.[57] The combined stretchability and breathability of the solidified inks limited the resistance change to less than 25% after heavy exercises (16 10-min jumping jack sessions during 4 h) for both electrode and interconnect traces on the forehead, demonstrating sufficient stability despite sweat (Figures 2E and S15). Human skin fibroblast cells cultured on the dried inks became fiber shaped and showed proliferation over time (Figures 2F–2H) comparable to the control (Figure S16), demonstrating the biocompatibility of the e-tattoos. Furthermore, no skin discoloration was observed after 6 h of electrode or interconnect coverage (Figure S17).

The printed and dried electrode and interconnect can withstand repeated deformation, owing to their low modulus, high stretchability, and good adhesion with skin (Figure 2I; Video S5). However, the inks can be easily removed with soapy water or alcohol wipes (Video S5).

Conventional EEG recordings are typically conducted using elastic caps with pre-arranged openings for gel injection in accordance with the international 10–20 system.[4] However, variations in head shapes can frequently cause suboptimal electrode positioning and insufficient contact between certain regions of the cap and the scalp, resulting in noisy signals or complete loss of signal.[1,58] Such issues can be eliminated by personalized sensor design and cap-free electrode placement (Note S6). First, a 3D scanning app (ScandyPro) on an iPhone 13 mounted on the 5-axis robot revolves around the participant's head to generate an unstructured triangulated surface representation of the head. We then define the electrode coordinates on this scanned head surface using an open-source function in MATLAB called MeshEEG.[59] For generic components with small dimensions, such as the electrodes with a selected diameter of 1.5 cm, it is sufficient to project a 2D template pattern (e.g., zigzag shown in blue in the upper left corner of Figure 3A) onto the target area in the mesh element plane. The straightforward nature of this printing path is facilitated by the robustness of the non-contact microjet printing method (Table S3; Note S2), allowing deposition to proceed unaffected by minor changes in the distance from the nozzle to the skin surface. This is not the case for typical continuous extrusion printing, where any hair obstruction or small changes in the nozzle-to-surface distance can easily disrupt the ink trace. In addition, the low-profile microjet nozzle is safer for on-body printing than the long and sharp needles used in typical extrusion printing.

Given the significant length (ranging from 5∼30 cm for a typical 10–20 montage) required to route the interconnects from the electrodes to the back of the neck where the amplifier is attached, a different approach is adopted to design the layouts of the interconnects. The algorithm identifies the intersections between the meshed scalp and the plane encompassing the electrode, its terminal at the back of the neck, and an intermediate point (e.g., C_4, T_{C4}, and I_{C4} in Figure 3A), detailed in Note S6 and Figure S18. The overall electrode-interconnect design algorithm is therefore referred to as the project-and-slice algorithm.

After pose matching the digital head model with the physical head position via three fiducial markers on the head, the algorithm converts the electrode-interconnect toolpath into a series of control commands (G-code) for the 5-axis robot (Figures 3B and S19). The algorithm plans the position and orientation of the robotic end effector so that the jetting axis is perpendicular to and at a fixed distance from the target surface. Should there be major head movement during printing, the G-code is regenerated based on the updated coordinates of the fiducials.

To assess the precision of our printing method, we performed a second 3D scan after printing and measured the offset of the central position of the printed electrode compared with its designed location (Figure 3C). The average deviation was ∼4 mm, with a maximum error less than 8 mm (Figure 3D). The error mainly stems from the limited accuracy of the 3D scan of the head shape through an elastic cap (not the electrode cap) used to suppress the hairs and smooth the surface. For medical applications such as epilepsy diagnosis, more precise head models constructed from X-ray tomography or magnetic resonance imaging (MRI), typically used in conjunction with EEG,[60] can be incorporated to further enhance electrode placement accuracy. Furthermore, regression and machine learning techniques may improve the accuracy of head shape prediction despite hair coverage.[61,62]

In a study measuring the channel impedance across 10 locations for each of the five subjects (Figures 4A and S20), the on-scalp printed electrode-interconnect e-tattoos showed a significantly lower average impedance (24.6 ± 22.0 kΩ) than traditional wet saline gel electrodes (53.3 ± 37.8 kΩ), with a notable statistical

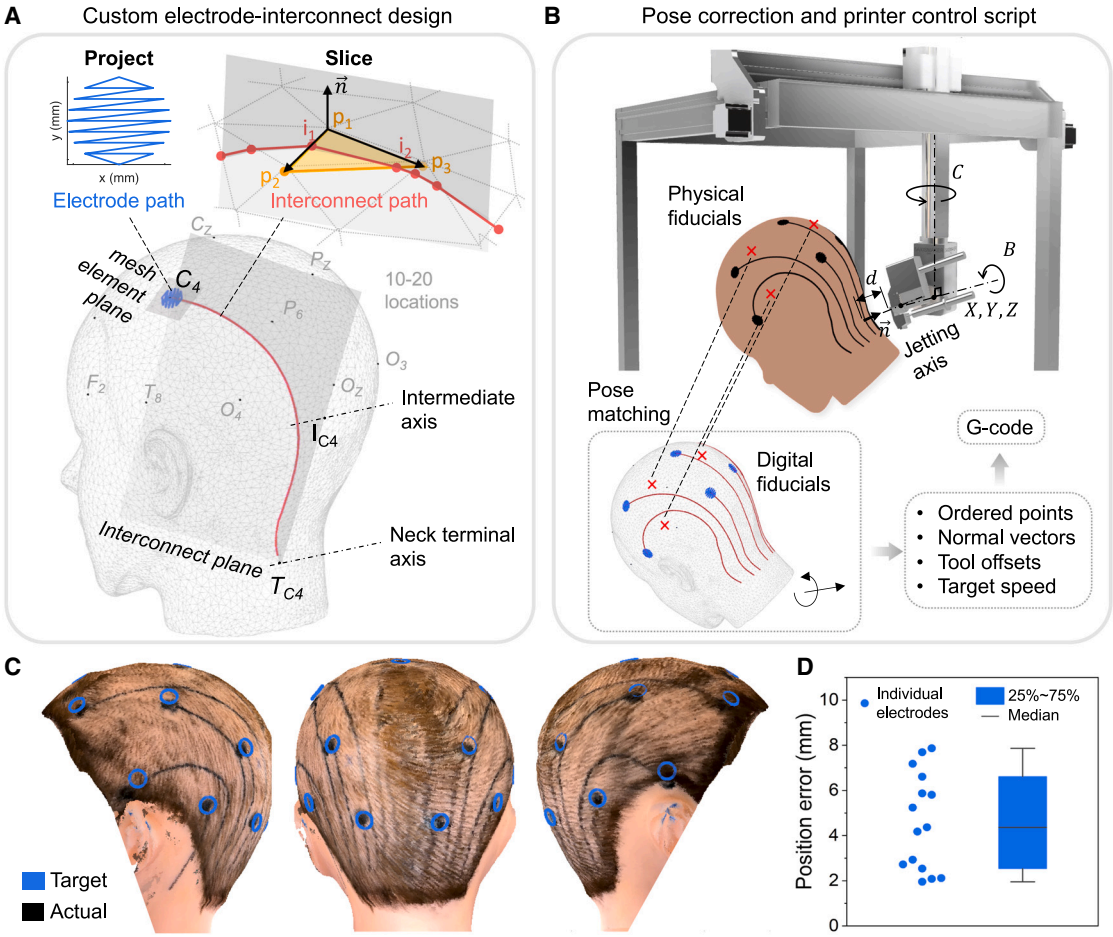

Figure 3. Method for the personalized design and printing of electrodes and interconnects on human heads in accordance with the international 10–20 system

(A) Project-and-slice algorithm to generate a custom electrode-interconnect array on a 3D triangular mesh model of the scanned head. The electrode (in blue) is projected from a 2D path template onto the 10–20 locations. The interconnect (in red) is generated by slicing the mesh with a plane encompassing the electrode (e.g., C_4), its corresponding terminal (T_{C4}), and an intermediate point (I_{C4}).

(B) The post-processing algorithm aligns three fiducial points on the digital model with those on the physical head to match the poses and generates control instructions (X, Y, Z, B, C) for head-conformable printing with the jetting axis normal to the scalp ($\vec{n}$) and at a fixed distance (d).

(C) Assessment of the printing accuracy on a hairy mannequin. The intended electrode locations (in blue) are overlaid with a 3D scan of the scalp post-printing (black electrode and interconnect traces).

(D) Distance between the printed and intended electrode positions across different EEG channels (circles correspond to individual electrodes, and the boxplot shows statistical metrics). The error bar indicates the minimum and maximum deviations. See also Figures S18 and S19.

difference ($p < 0.0001$). This lower and more uniform impedance across the board is critical for recording high-fidelity EEG data in ambulatory conditions where temperature fluctuations, EMI, and motion-induced changes in skin potentials are not controllable.[43,63,64] The smaller variation in the impedance of the printed electrodes compared with gel electrodes proves that the microjet printing through the hairs and over the curved surface of the head is robust and repeatable. After 6 h, the performance of the gel electrodes deteriorated drastically, with 37% of the channels unmeasurable and most of the remaining ones showing impedance values above 200 kΩ, which is considered unsuitable for EEG (Figure 4B, Note S3). By contrast, the on-scalp printed electrodes and interconnects maintained a stable impedance below 40 kΩ even after 6 h. As expected, the skin-electrode interface dominates the channel impedance, with only a minor contribution from the interconnect trace (stable routing resistance 2 < kΩ for 6 h, Figure S21). To limit EEG recording to the electrode site and inhibit signal pickup along the interconnect, the interconnect ink was designed to provide high contact impedance (Figure S22; Note S4). It was confirmed that no meaningful difference was observed between the EEG recorded using an electrode routed with an interconnect in direct contact with the skin versus an electrode routed with an interconnect printed on top of a thick electrically insulating latex layer (Figure S23). EEG recording during head-turning movements was equivalent between gel and printed electrodes (Figure S24). Both freshly applied gel and printed electrodes

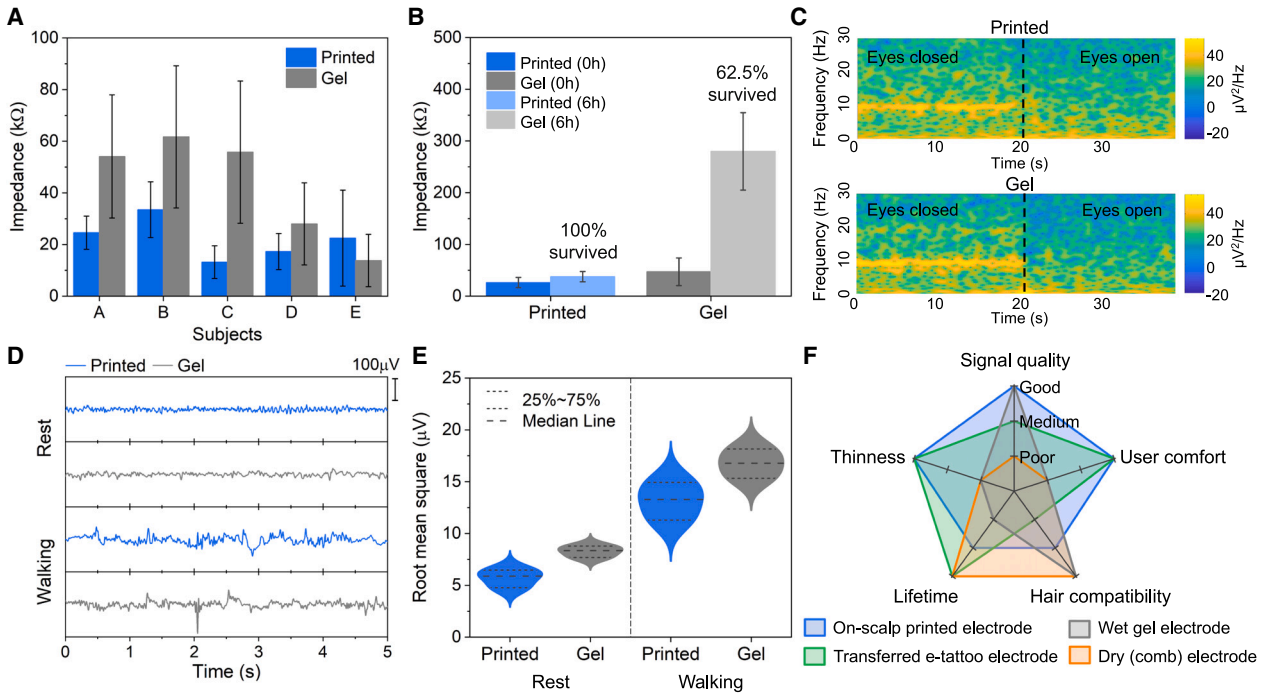

Figure 4. EEG recording performance of the on-scalp printed electrodes benchmarked against commercial wet-gel electrodes

(A) Average contact impedance of 10 printed (in blue) and gel (in gray) electrodes on each of the five subjects right after application, i.e., at 0 h. The printed electrodes have low impedance with a narrow distribution across subjects and scalp locations, whereas gel electrodes show higher average impedance with greater variability.

(B) Comparison of the average contact impedance of all subjects at 0 h and after 6 h confirms that gel electrodes are unsuitable for long-term EEG (27.5% are disconnected, and the remainders show exceedingly high impedance, i.e., over 200 k Ω). In comparison, all printed electrodes maintain low impedance after 6 h. Error bars indicate one standard deviation.

(C) EEG spectrograms confirm the presence of the expected alpha wave (10 Hz) with eyes closed for both printed and gel electrodes.

(D and E) EEG waveforms and root mean square values during rest and motion are comparable between printed and gel electrodes.

(F) A comparative evaluation of various types of EEG electrodes (on-scalp printed, transferred e-tattoo, wet gel, and dry comb) across several metrics (signal quality, thinness, electrode lifetime, user comfort, and hair compatibility) shows that on-scalp printing is the only technology without any major drawbacks (rating criteria in Table S4). See also Figures S20–S24.

successfully detected alpha waves when participants closed their eyes (Figure 4C), and both types recorded comparable signals during rest or walking states (Figures 4D and 4E). The advantages of on-scalp printing technology compared with alternatives are evident in a radar chart (Figure 4; rating criteria in Table S4). The on-scalp printed e-tattoo technology merges the hair-friendly and low contact impedance features of wet-gel electrodes with the dry, sleek benefits of e-tattoos, all while being a cost-efficient and time-saving method of digital production.

To assess the stability and effectiveness of the printed electrodes and interconnects in capturing specific EEG signals over time, under institutional review board (IRB) approval, we performed sensor printing and EEG measurements on five different participants, focusing on two popular BCI markers: motor imagery (MI) and error-related potential (ErrP) (Figure 5A). Eight electrodes over the motor cortex and medial line (Figures 5B and S25) recorded each EEG marker under three experimental conditions: with fresh gel electrodes (gel-0 h), freshly printed electrodes (printed-0 h), and printed electrodes after 6 h of wear (printed-6 h). Due to the ineffectiveness of gel electrodes after 6 h (Figure 4A), no EEG could be measured.

We evaluated signal quality in MI-based BCI experiments by analyzing the number of rejected 1-s EEG samples. A single-factor repeated measures analysis of variance (ANOVA) revealed no statistically significant difference among the three conditions (p = 0.2018; printed-0h: 8.53 ± 0.78%, printed-6 h: 15.55 ± 11.83%, gel-0 h: 8.18 ± 0%; Figure 5C). In particular, the group means for fresh gel and freshly printed electrodes were similar, with only ~10% of all acquired samples being rejected. A slightly higher rejection rate was noted in the printed-6 h condition, likely attributed to deteriorated terminal-to-cable connection at the highly deformable back of the neck given the previously confirmed stable electrode-interconnect contact impedance after 6 h.

We also quantified the event-related desynchronization (ERD) over the motor area contralateral to the right hand during the MI task (three channels on the left lobe). All three conditions showed a desynchronization effect (Figure 5D); printed-0 h: − 37.82 ± 16.17%, printed-6 h: − 37.60 ± 10.35%, and gel-0 h: − 35.04 ± 7.19% with no significant differences found (p = 0.8305). Additionally, we observed a stable trend in the ERD captured by the printed electrodes during the two recording

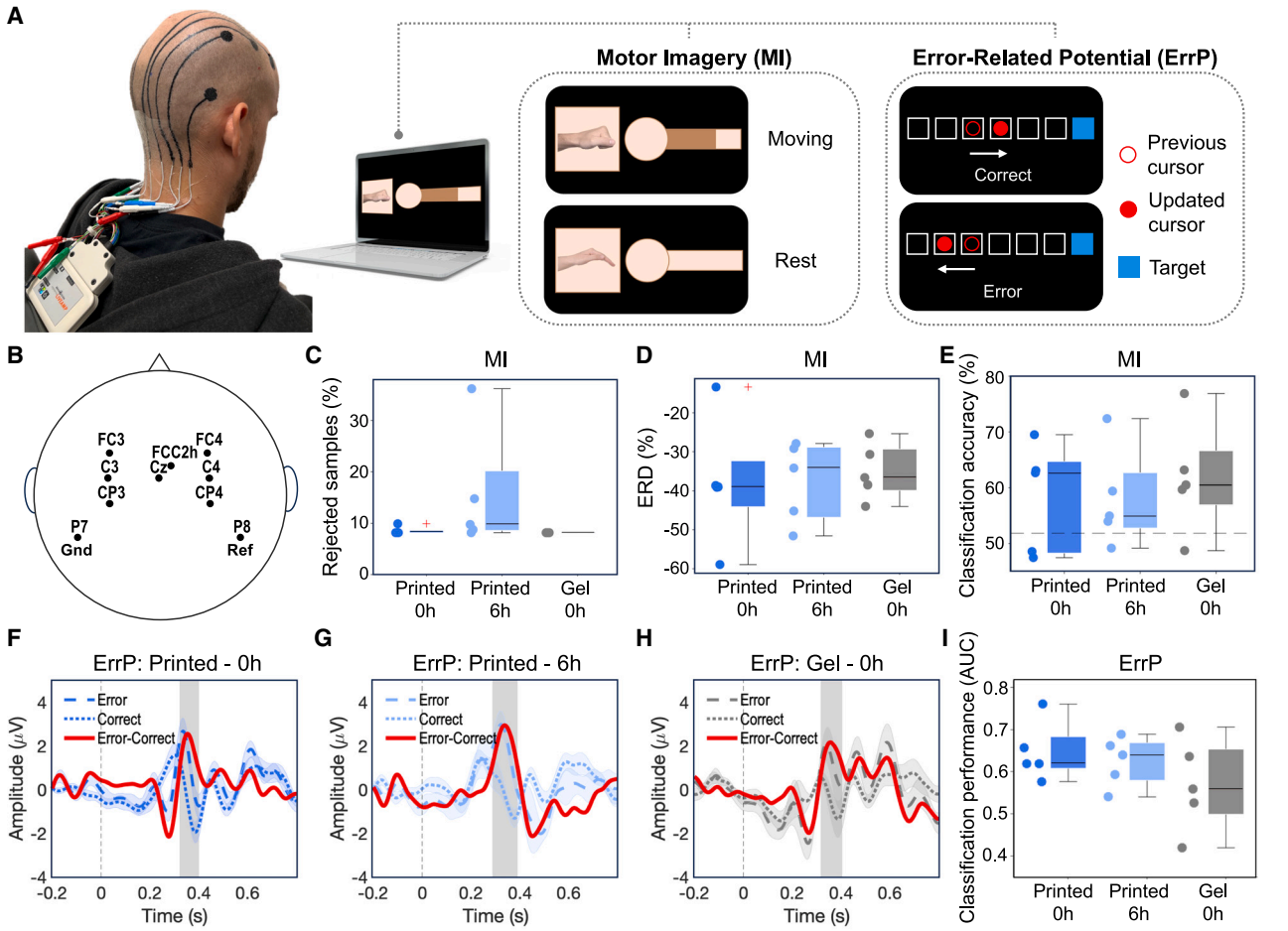

Figure 5. BCI performance of printed electrodes (immediately and 6 h post-printing) compared with conventional wet-gel electrodes immediately after application because they become unusable after 3∼5 h

(A) A photo of printed electrodes and interconnects connected to BrainVision amplifier and illustrations of experiments to elicit the two EEG markers: MI and ErrP.

(B) Printed EEG electrode montage.

(C) Fraction of 1-s EEG samples rejected during MI trials.

(D) Event-related desynchronization (ERD) observed in MI trials.

(E) Accuracy of MI classification based on leave-one-run-out cross-validation.

(F–H) Grand-averaged ErrP.

(I) Classification performance of ErrP using leave-one-block-out cross-validation. In the boxplots, the central line indicates the median, the box bottom and top edges indicate the 25th and 75th percentiles, respectively, and the whiskers extend to the maximum and minimum values. See also Figure S25.

sessions. For the performance assessment of the MI-based BCIs, cross-validation analysis was conducted for each condition (Figure 5E). The mean classification accuracy among different participants under all conditions (printed-0h: 58.23 ± 9.74%, printed-6h: 57.97 ± 8.84%, gel-0h: 61.78 ± 10.08%) outperformed chance level (51.83%) with no significant differences among them (p = 0.7849). Although we observed MI performance lower than chance for some subjects under some conditions, the literature has shown that MI-BCI is a user-in-the-loop system and requires longitudinal user training over multiple days to acquire the skills necessary to operate it reliably,[65,66] which was not performed in our protocol.

Figures 5F–5I illustrate the grand-averaged ErrP across all trials of all subjects at the Cz channel with respect to the stimulus onset. ErrPs are characterized by the time-locked components of positivity and negativity relative to cue onset.[67,68] Gray shaded zones denote the time window in which the cluster-based permutation test of the individual block-wise averaged error and correct trials with Benjamini-Hochberg correction resulted in p values below 0.05. Our analysis demonstrates similar significant temporal windows in all three conditions—printed-0h, printed-6h, and gel-0h—where error positivity around 0.4 s was observed. Classification analysis of the ErrP data from individual subjects resulted in the classification performance of the area under the curve of 0.65 ± 0.070, 0.62 ± 0.059, and 0.57 ± 0.11 for each condition, respectively (Figure 5I). No significant differences in classification accuracy were found between the three conditions (p = 0.44).

The analysis across the two EEG markers demonstrates that our printed electrodes perform comparably to standard gel electrodes. Additionally, compared with conventional wet-gel electrodes, the printed electrodes extended the electrode lifetime to at least 6 h and ensured consistent performance over multiple sessions.

DISCUSSION

On-scalp e-tattoo printing has the potential to drastically shorten the EEG setup time. In our study, 3D head scanning and printing of 10 electrodes can be completed within about 15 min. However, head movements require additional calibration to update the coordinates of the landmarks, adding an extra 5 min per movement. Hence, incorporating visual tracking systems into the printer to create a closed-loop control can enable faster on-scalp manufacturing. Note that although the current on-scalp printing process requires a time commitment of the participant, it is time- and cost-saving compared with the conventional microfabricated e-tattoos in addition to the benefits of personalization, hair compatibility, and large-area coverage. More work is needed to scan and print on heads with long and thick hairs. Highlighting the persistent issue of racial bias in neuroscience research is crucial, as traditional EEG electrodes are often unreliable on individuals of African descent, resulting in suboptimal patient experiences and outcomes in clinical settings.[69,70] Curly hairs tend to push against the EEG cap, reducing contact between the electrodes and the scalp, leading to a poor contact impedance.[71] Developing on-scalp digital printing for different hair types should prioritize bridging this important gap.

E-tattoos must retain their form and functionality when exposed to external factors such as abrasion to be effectively used in applications such as sleep monitoring and to integrate seamlessly with other head-wearable devices, such as virtual reality (VR) headsets and protective helmets.[72] Thus, further enhancing the adhesion between the printed e-tattoos and the scalp skin without complicating its removal is an important future research direction. Other opportunities include on-scalp printing of diverse ink types, such as semiconductors and dielectrics[40,73] for operational amplifiers, enabling active signal amplification similar to existing active EEG electrodes based on rigid electronics.

In a broader sense, the introduced method for on-body digital printing addresses the persistent issue of traditional e-tattoos not being compatible with extensive regions of intricate 3D or hair-covered skin surfaces. Over the years, despite rapid progress in functionalities and wearability, e-tattoos have remained costly to fabricate, small in size, and restricted to relatively flat and glabrous skin surfaces.[13,14,16] Surmounting these limitations will allow for spatial mapping of physiological signals across extensive and curved body surfaces. This advancement is appealing for numerous applications beyond EEG, such as electromyography (EMG) and transcutaneous electrical nerve stimulation (TENS), pertinent to human-machine interfaces, performance training, and rehabilitation. Moreover, it possesses the capability for sensor integration on internal organs, such as on the cranium for electrocorticography (ECoG) recordings,[74] on the heart for electrocardiogram (ECG) monitoring or stimulation,[75] to aid in wound healing,[32] and on tissue or bone for regeneration purposes.[76–78] Ultimately, it opens the door for the on-body integration of sensing, processing, communication, and power components tailored specifically to the anatomy and needs of the user.[79,80]

In summary, we have developed a safe digital printing method that allows for the direct creation of customized, ultrathin, stretchable, and skin-conformal e-tattoos on a hairy scalp. These e-tattoos are electrically conductive and mechanically, as well as physiologically, unnoticeable, offering full-head, high-fidelity, long-term, and comfortable EEG recording capabilities without the need for labor-intensive and short-lived wet-gel electrodes, as well as cumbersome cables and caps. The specialized electrode and interconnect inks allow for microjet printing, self-drying, and high-fidelity EEG recording from specific sites. Additionally, a tailored project-and-slice algorithm streamlines the personalized electrode-interconnect layout design in adherence to international standards. The system has been validated against traditional gel electrodes used with EEG caps. This innovation significantly expands the potential applications of e-tattoos for EEG by solving many long-standing challenges. It marks a new chapter in neurotechnology, emphasizing customization and accuracy, enhancing patient well-being, and minimizing healthcare labor.

EXPERIMENTAL PROCEDURES

Ink formulation

Poly(3,4-ethylenedioxythiophene):poly(styrene sulfonate) (PEDOT:PSS) (ICP 1050, 739332, Sigma-Aldrich) was freeze-dried using liquid nitrogen and a Labconco FreeZone 1 Freeze Dryer. To make the electrode ink, 11.6 mg NaCl (S271, Fisher), 60 mg dried PEDOT:PSS, and 60 mg glycerol (AA36646, Fisher) were added to 2 g deionized (DI) water. To make the interconnect ink, 60 mg dried PEDOT:PSS, 60 mg glycerol, and 120 mg DMSO (D128, Fisher) were added to 2 g DI water. A glass rod was used to thoroughly mix the ingredients. A 4°C fridge was used for long-term ink storage.

Ink characterization

Tensile tests

The inks were dried in molds made of Ecoflex 00-30 (Smooth-on). Then, the dry films were tested by a dynamic mechanical tester (DMA 850, TA Instruments) under a strain rate of 0.05/min. The film thicknesses, 15∼20 μm, were determined by scanning electron microscopy (SEM). The stiffness at 1% strain was used for modulus calculation.

Conductivity measurements

The inks were dried in molds made of Ecoflex 00-30 (Smooth-on). Then, the dry films were tested by electrochemical impedance spectroscopy (EIS) mode using a CHI660e electrochemical workstation. The resistance does not change with frequency, indicating the dried inks are electrically rather than ionically conductive. The thicknesses were determined by SEM.

SEM images of films on skin phantom

First, a reverse mold of the skin was made by pouring Ecoflex 00-30 (Smooth-on) on the forearm of the author and waiting for 30 min for curing. Then, Ecoflex 00-30 was poured on the reverse mold to form the skin phantom. Before making the skin phantom, the reverse mold was treated by chemical vapor deposition using trichloro(1H,1H,2H,2H-perfluorooctyl)silane (448931, Sigma-Aldrich) to ensure the successful detachment of the skin phantom from the reverse mold. The ink was dried on a flat glass substrate, which was then transferred to the skin phantom. For the transfer-on-skin film, the ink was also applied on a separate piece of skin phantom with controlled mass, which will yield a film with the same mass per area as the transferred-on film. The SEM images were taken using a Zeiss Supra 40VP SEM.

Peeling force tests of the inks on porcine skins

Porcine skins were purchased from a supermarket and were glued on a glass substrate using superglue. Both electrode and interconnect inks were tested for two conditions: (1) the inks were dried on a flat glass substrate and then transferred to the porcine skin, and (2) the inks were deposited directly on porcine skin in controlled amounts to yield a film with the same mass per area as the transferred-on film. The peeling test was done using a UStretch tensile test machine from CellScale. Scotch Super 33+ tape was used as the backing during the peeling test (Figure S26). The data reported in Figure 1F were the average values from the stable peeling region when no tearing happened.

Ink contact angle measurements

100 μL of ink was placed on various surfaces to form a droplet at room temperature. The figures are taken by camera (FL3-U3-13Y3M-C, Point Gray) with a micro-image lens (Zoom 125, OPTEM) and processed by ImageJ software.

Ink viscosity measurements

The viscosity was measured by a rheometer (HR30, TA Instruments) equipped with 25 mm parallel plates with a 1-mm gap. The tests were done at room temperature.

Electrical properties under mechanical strain and stability tests

The interconnect and electrode ink were casted on a 1-mm-thick polydimethylsiloxane (PDMS) substrate through a medical tape mask and dried at room temperature. Then, the mask was removed, and the PEDOT:PSS film with a width of 5 mm and a length of 20 or 10 mm was obtained. The thickness of the sample is 30 μm. Two copper traces with 1 mm in width were attached to the two ends of the PEDOT:PSS film through silver paste. Next, the sample was dried on a hotplate at 90°C for 10 min. After this, the silver paste at the two ends was encapsulated with half-cured PDMS and cured in an oven of 70°C for 30 min. The specimen was fixed on a dynamic mechanical analyzer and stretched at a speed of 0.1 mm/s. The resistance was simultaneously recorded with an inductance-capacitance-resistance (LCR) meter (3532–50 LCR HiTester, Hioki). The repeated stretching was tested under oscillation mode at a strain of 10%, and the oscillation frequency was 0.5 Hz.

Skin interfacial impedance tests

EIS was used to characterize the skin-electrode interfacial impedance of different electrode materials across the frequency range of 0.1 to 1,000 Hz (Autolab, Metrohm). In addition to our electrode ink, three commercial gels were characterized: saline wet-gel (Signagel, ParkerLabs), non-saline wet-gel (Spectra 360, ParkerLabs), and solid-gel button electrodes (Kendall H124SG 1″, Corvidien). For Note S4, we also test a commercial water-based carbon ink (Electric Paint, Bare Conductive) and a silver ink. The silver ink fabrication followed the procedure in Zhu et al.[31] by first dissolving 2.5 wt % polyethylene oxide (PEO) (Mv 1,000,000, Sigma-Aldrich) in 1:4 water:ethanol solution and then adding silver flakes (10 μm, Sigma-Aldrich) such that the dry ink weight ratio is 9:1 Ag:PEO. The forehead of the subject was first cleaned with a soft alcohol wipe (alcohol prep pads, CareTouch), without any abrasion. A pair of each type of electrode was then applied to the forehead. For the wet-gel and ink electrodes, stickers with a circle cutout in the center (washers, inner diameter 8 mm, BrainVision Solutions Inc) were used to delimit the area and ensure consistent coverage. Standard EIS measurement was carried out, and the measured impedance was normalized by the electrode area.

Skin conformability mechanical analysis

The mechanical analysis of the printed and transferred e-tattoo skin conformability for both electrode and interconnect inks (Figure S27) was carried out using the energy minimization method by Wang and Lu[81] as detailed in Note S5.

Sweat stability measurements

Both inks were applied on the forehead of a test subject and let dry. A sweat patch (Figure S15) was affixed to adjacent skin, and an exercise session was conducted to stimulate sweat production. The exercise consists of 10-min sessions of jumping jacks followed by 5-min breaks for 4 h at room temperature, performed by a female researcher. The resistance before and after the exercise was measured by EIS mode using a CHI660e electrochemical workstation.

Breathability of electrode and interconnect films

The water vapor transmission rate (WVTR) of the electrode and interconnect films was measured based on ASTM E96. Briefly, the ink of the electrode or the interconnect was poured onto an Ecoflex mold and was dried on a hotplate at 50°C for 15 min. After the film was fully dried, it was peeled off from the Ecoflex mold, and a free-standing film of electrode or interconnect with a thickness of ~30 μm was obtained. Then the film was used to seal a glass bottle filled with 0.5 g DI water with a rubber band to fix the film onto the glass bottle. Another glass bottle with DI water but no cover was used as the control sample. Finally, the bottles were put in a chamber with a temperature of 21.5°C and a humidity of around 35%. The samples were weighed at different periods for 7 days to measure the weight change of water. The WVTR was calculated by the water loss using the following formula:

$$WVTR = \frac{\Delta m}{AT} \quad \text{(Equation 1)}$$

where Δ m is the weight loss of water, A is the mouth area of the glass bottle, and T is the time.

Cell test

Cell preparation: skin fibroblast cells were obtained from a patient (UCLA institutional review board [IRB] number IRB#11-002778) and were propagated and maintained in the DMEM-F12 media (Dulbecco's Modified Eagle Medium, 11965092, Gibco) supplemented with 10% fetal bovine serum (FBS, 26140079, Gibco) and 1% Anti-Anti (antibiotic-antimycotic, 15240-062, Gibco). TrypLE (TrypLE Select Enzyme, 12563011, Gibco) was used as the dissociation reagent in the propagation step. Lentivirus transduction (PP7 Cherry, Plasmid #61763, Addgene) was carried out to make the cells fluorescent and resistant to the antibiotic puromycin. After the transduction, puromycin was used to kill the cells that were not transduced.

PEDOT:PSS film preparation: the electrode ink and the interconnect ink were applied to a 12-well plate and were dried in ambient to form polymer films at the bottom of the wells. The polymer films were soaked and washed three times with PBS/Anti-Anti, during which the 12-well plates were stored in a 4°C fridge. The 12-well plate was then placed in an incubator with DMEM/FBS for 3 days to test if the film was sterile. Before seeding the cells on the polymer films, they were washed three times with PBS/Anti-Anti (antibiotic-antimycotic [100×], 15240062, Gibco).

Seeding the cells: 50,000 of the transduced cells were added to each well of the 12-well plate with the PEDOT:PSS film substrate. A microscope (LSM 880, Zeiss) was used to acquire images of the cells (Figures S28 and S29). Cells directly cultured on a 12-well plate without adding any ink materials were used as a control. ImageJ software was used to outline the cells and calculate the percentage area of the cells in the entire field of view. For each sample, 2–3 fluorescent micrographs were analyzed. Because in all the experiments the cell seeding density and the field of view are the same, the percentage area can be used to reflect biocompatibility on various substrates.

Mechanical durability and removal of the on-skin-printed e-tattoo

The ink was printed on the forearm of a subject. The dried ink was subjected to mechanical torture, such as rubbing and twisting by human hands. Then, it was removed by wiping it with an alcohol wipe or soapy water.

Printer

A pneumatically actuated microjet tool (MDS 1560, VERMES Microdispensing GmbH) was used for non-contact ink dispensing using a 150-μm diameter nozzle at a frequency of six pulses per second, actuator pressure of 2.7 bars, and cartridge pressure of 1.7 bars. The microjet tool was integrated into a 5-axis robot system (5XM600, 5AXISWOKS LTD). The microjet dispensing and 5-axis motion (two rotational and three translational axes) were controlled via motion control software (Mach4, Newfangled Solutions) and programmed in G-code. The end-effector translation speed was capped at 200 mm/min. A custom G-code command was assigned to actuate a 24 V relay that signals the microjet controller (MDC 1500, VERMES Microdispensing GmbH) to initiate and end jetting. The 3D scanning of the scalp shape and neck used a commercial application (ScandyPro, Scandy) and was carried out by attaching a camera (iPhone 13, Apple Inc.) to the printer end effector and revolving 360° around the subject. During the scanning, the subjects used a tight-fitted elastic black cap with white cross-line patterns to aid with point tracking. This cap also compresses the hair against the scalp to assist in probing the correct scalp shape. Three holes in the cap were used to mark three fiducials on the subject's head

with a non-permanent maker (surgical skin marking pen, BrainVision LLC.). These three fiducial markers serve to match the digital head model with the physical head position. During scanning and printing, the subject sits on an adjustable massage chair with the face resting on the face pillow (Ergo Pro II, Stronglite). A 3D scan of the face is generated separately and merged with the 3D scalp scan using MeshLab to enable extracting the four reference point coordinates (nasion, inion, and left and right preauricular points) used in the 10–20 international standard for EEG placement.[4]

EEG recording

We enrolled a total of five healthy individuals (male, aged 25–45 years). Each participant carefully reviewed and signed the informed consent form, which had been approved by the University of Texas at Austin IRB (IRB number: STUDY00002937). Consent was obtained for the publication of the images of the participants. All EEG recordings were carried out with a 32-channel EEG amplifier (LiveAmp, BrainVision) as the data acquisition system and were filtered using a bandpass filter with a range of 1–40 Hz. The experiment consists of EEG recording using conventional wet-gel electrodes and the on-scalp printed EEG system. For wet-gel electrodes, commercial EEG caps were used with Ag/AgCl electrodes (Multitrodes, EasyCap) and commercial saline gel (Signa gel, ParkerLabs).

Skin preparation

The hair was washed with shampoo and water and then allowed to dry. The electrode locations were then cleaned using an alcohol gel wipe. Throughout all experiments, the skin was not abraded in any way.

Terminal connections

First, a skin-safe glue (Spirit Gum, Mehron Makeup) is applied to the terminal locations and left for a few minutes until tacky. The 1.5-mm touch-proof carbon fiber connectors (AUVON TENS) were then placed over the glue, and a trace of interconnect ink was manually deposited to bridge the printed traces with the carbon fiber terminals. This ensured a secure and reliable electrical connection between the tattoo-like printed interconnects and the terminal connector.

Electrode impedance measurements

All five subjects participated in the impedance measurements using the commercial wet-gel and on-scalp printed electrodes. The standard 10–5 system[82] was used for the placement of 10 electrodes (Figure S25). The same five subjects, number of electrodes, and EEG amplifier were used for both electrode types (i.e., manually applied commercial wet gel and on-scalp printed e-tattoo). The impedance was measured by the amplifier connected to the neck terminal at the standard frequency of 15 Hz. The impedance was measured twice, one at 0 h and another after 6 h of electrode placement. For wet-gel recordings, an EEG cap was used, and the recording was conducted immediately after applying the wet gel. For printed electrodes, the recordings were taken after the prints had fully dried on the scalp.

Motion artifact

For the motion artifact test, the subjects were instructed to carry out the following sequential movements: "head up," "head down," "head left," "head right," "swallow," and "jaw clench," while the electrical signals were recorded by the amplifier connected to the neck terminal. We analyzed the recordings of two channels (C3 and C4) during these movements (Figure S24). Additionally, the subjects were instructed to sit and walk, and the root mean square of the recordings was calculated (Figure 4E).

Interconnect insulation validation

A custom print was carried out on the freshly washed scalp (no abrasion) of one subject using the following configuration: only the interconnect is printed for C5 and P3; both interconnects and electrodes are printed for FCC1h, FCC2h, Cz, Pz, P4, C4, and C6. For FCC2h, a thick layer of electrically insulating material (Liquid Latex, Mehron) was manually applied to the skin along the interconnect routing path before printing the interconnect ink on top. The impedance and EEG signals were measured by the amplifier (LiveAmp, BrainVision) connected to the neck terminal (Figures S22 and S23). 1-min length (3,000 samples per channel) of alpha-bandpass (8–12 Hz) filtered signals during sessions of eyes open and closed were analyzed using mutual information analysis to quantify the relationship between a pair of electrodes. High MI values can indicate a higher level of shared information between the channels, whereas low values indicate greater independence.

BCI recording

During all the experimental sessions, we captured neural activity at eight locations in the 10–5 system[82] plus the reference and ground electrode near the mastoids. The choice of electrode positions was based on the prominent regions associated with neural markers related to two validated BCI modalities: MI[83] and error-related potential (ErrP)[67]. The positions for the on-scalp printed electrodes were CP3, C3, FC3, Cz, FCC2h, FC4, C4, and CP4. FCC2h was used instead of FCz for easier interconnect routing using our design algorithm (Note S6). P7 and P8 were the reference and the ground. For the gel electrodes, the closest available positions were selected from a cap with standard built-in electrodes (32ch BrainProducts EasyCap), which were FC5, C3, CP5, Cz, FCz, FC6, C4, and CP5. TP9 and TP10 served as the ground and reference. Figure S25 shows the montage schematic and photos of both setups.

Motor imagery

Experimental protocol. During the experiment, participants were instructed to either mentally imagine flexing their right hand (RH-MI class) without actually performing any physical movement or to remain in a resting state and avoid any specific thoughts (rest class). We employed a standard bar feedback-based offline session paradigm[84] to acquire the MI signals. Each session, whether using printed or gel electrodes, consisted of multiple runs. In each run, the participants performed 10 trials, with each trial belonging to either the RH-MI class or the rest class. The order of the trials was randomized. The trials followed a specific sequence. First, a fixation cross was presented for 2 s, during which the participants were instructed to prepare for the upcoming cue. This was followed by the presentation of a cue (either rest or RH-MI) for 1.5 s. After the cue presentation, the participants were presented with visual feedback in the form of a moving bar or circle. The feedback was displayed for 5 s and guided the participants based on the targeted cue. Specifically, a moving bar or circle appeared on the corresponding side of the targeted cue (Figure 5A). The circle represented the resting state, whereas the rectangle represented the RH-MI class. The trial concluded with a 2-s presentation of the trial result, followed by a 1.5-s inter-trial rest period before the start of the next trial.

Motor imagery characterization. We used state-of-the-art minimum distance to mean (MDM) Riemannian geometry classifier (RGC) for motor imagery decoding.[65,85] RGC uses covariance matrices of bandpass-filtered multi-channel EEG data as features for MI signal classification. In brevity, positive definite covariance matrices reside on the Riemannian manifold, which can be embedded using the affine invariant Riemannian metric (AIRM). The AIRM allows for defining the concept of Riemannian distance on the manifold, which is utilized in training the MDM classifiers. Refer to Yger et al.[86] for a detailed description.

To obtain an unbiased estimation of the classification performance, we employed a leave-one-run-out cross-validation (LOROCV) strategy. This involved using all runs except one as training data to build the classifier and then evaluating the performance on the left-out run. This process was iterated for each run, and the average classification performance across all runs was reported. After recording the signals, we visually inspected all the channels and rejected the EEG data from channels that appeared as flatlines or recorded exceptionally high amplitudes. For LOROCV analysis, we bandpassed the signals in [8–30] Hz and used 1-s samples with 0.05-s step size. In all MI-BCI analyses, we further discarded samples in which any data point within the 1-s segment exceeded an absolute value of 100 μV. To characterize the signal quality, we estimated the fraction of samples out of total of 1-s samples during the task period that were not rejected according to the earlier mentioned rejection criteria.

For the ERD analysis, we calculated the baseline power ($p_{c,t}^{rest}$) using a 1-s window from the fixation period. Subsequently, the task power ($p_{c,t}^{task}$) was estimated using non-overlapping 1-s windows beginning 0.5 s after the presentation of the cue. We excluded the initial 0.5-s period after the task presentation to avoid the influence of visually evoked potentials. We then estimated the ERD value for a trial t of c^{th} channel as

$$ERD_{c,t} = \frac{p_{c,t}^{rest} - \underset{n \in (1,5)}{\operatorname{argmin}}\, p_{c,t}^{task}}{p_{c,t}^{rest}} \quad \text{(Equation 2)}$$

where n is the number of non-overlapping windows during the task period (in our current experiment, n ranges from 1 to 5).

ErrP

To test whether our proposed system could be used for ErrP detection, we collected 8-channel EEG data from four runs of visual ErrP tasks in five subjects. In these tasks, the subjects were instructed to monitor the cursor movement and evaluate if the cursor moved toward a target position (marked in red) correctly or erroneously. The subject had no control over the cursor movements, and the cursor moved horizontally every 2,000 to 2,500 ms across a 1D space composed of 10 positions (Figure 5A). The cursor moved away from the target with a 30% chance of the trials. When the cursor reached the target position, a new target location was chosen randomly.

We performed event-related potential (ERP) and classification analysis on ErrP data following these steps. EEG data from four blocks for individual subjects were concatenated and bandpass filtered between 1 to 10 Hz using a non-causal fourth-order Butterworth filter. Time samples from the time window (−1.3 s before to until 1.5 s after stimulus onset) were chosen and segmented as epochs. Baseline correction was applied using the 100 ms window prior to stimulus onset. Trials that contained time points above the absolute value of 50 μV in any channel were rejected from epochs. ERP analysis was performed by averaging all of the epochs from all subjects with respect to error and correct conditions. In the classification analysis, we used the window [0.2, 0.8] s after the onset of the cursor movement, downsampled to 64 Hz. Features corresponded to the EEG voltage of each time sample and the power spectral density (PSD) between 1–10 Hz from all eight channels. Features were min-max normalized to values between 0 and 1. The classification accuracy was computed using leave-one-run-out run-wise cross-validation from the four blocks, using diagonal linear discriminant analysis (LDA).

RESOURCE AVAILABILITY

Lead contact

Further information and requests for resources and reagents should be directed to and will be fulfilled by the lead contact, Nanshu Lu (nanshulu@utexas.edu).

Material availability

This study did not generate new, unique materials.

Data and code availability

The authors declare that the data supporting the findings of this study are available within the article and its supplemental information files as well as from the corresponding author upon reasonable request. The algorithm for custom electrode-interconnect layout design and G-code generation is available at: https://doi.org/10.5281/zenodo.14015242.

ACKNOWLEDGMENTS

N.L. acknowledges the support from the US Army Research Office under Cooperative Agreement W911NF-19-2-0333. The views and conclusions contained in this article are those of the authors and should not be interpreted as representing the official policies, either expressed or implied, of the US Army Research Office or the US government. X.M. and M.G.M. acknowledge the support of the National Institutes of Health (NIH) R01 award DK132319-02, American Society of Chemistry Petroleum Research Funding PRF# 66747-ND7, and the Johnson & Johnson WISTEM2D Scholars Program Award. J.d.R.M. acknowledges support from the Coleman Fung Foundation.

AUTHOR CONTRIBUTIONS

N.L. designed the research. L.S.d.V., N.L., E.W., and C.B. conceived and implemented the 5-axis on-scalp microjetting platform. S.T., E.L., and L.S.d.V. wrote the electrode-interconnect design and printer control algorithms. H.L. and P.V. carried out ink breathability experiments, interconnect insulation validation study, and film conformability cross-section measurements on porcine skin. Y.Y., B.Y., X.H., L.S.d.V., and N.L. carried out the ink development. W.H. carried out sweat stability and contact angle measurements. Z.L. carried out the mechanical analysis of skin conformability using the energy minimization method. Y.Y., B.Y., L.S.d.V., P.M., S.D., and E.W. characterized the electrical and mechanical properties of the interconnect and electrode inks. Y.Y., Y.D., R.S.S.-V., and M.G.M. characterized cell biocompatibility. S.K., M.Z., F.I., and J.d.R.M. designed the BCI experiments. P.M., M.Z., S.K., E.L., A.T.R., P.T., and P.W. carried out BCI experiments, including human subject preparation, head scanning, printing, and analysis. L.S.d.V., Y.Y., S.K. M.Z., H.L., P.M., S.D., Z.L., P.V., P.T.T., J.d.R.M., X.H., and N.L. wrote the paper.

DECLARATION OF INTERESTS

N.L. is on the advisory board of *Cell Biomaterials*. J.d.R.M. is a consultant for Meta Reality Labs Research.

DECLARATION OF GENERATIVE AI AND AI-ASSISTED TECHNOLOGIES IN THE WRITING PROCESS

During the preparation of this manuscript, the authors used TexGPT only to polish the language. After using this tool, the authors reviewed and edited the content as needed and take full responsibility for the content of the publication.

SUPPLEMENTAL INFORMATION

Supplemental information can be found online at https://doi.org/10.1016/j.celbio.2024.100004.

Received: September 16, 2024
Revised: October 25, 2024
Accepted: November 1, 2024
Published: December 2, 2024

REFERENCES

1. Michel, C.M., Murray, M.M., Lantz, G., Gonzalez, S., Spinelli, L., and Grave de Peralta, R.G. (2004). EEG source imaging. Clin. Neurophysiol. *115*, 2195–2222. https://doi.org/10.1016/j.clinph.2004.06.001.
2. Niedermeyer, E., and da Silva, F.L. (2005). Electroencephalography: Basic Principles, Clinical Applications, and Related Fields (Lippincott Williams & Wilkins).
3. Ramsey, N.F. (2020). Human brain function and Brain-Computer Interfaces. Handb. Clin. Neurol. *168*, 1–13. https://doi.org/10.1016/B978-0-444-63934-9.00001-9.
4. Jasper, H. (1958). Report of the committee on methods of clinical examination in electroencephalography. Electroencephalogr. Clin. Neurophysiol. *10*, 370–375. https://doi.org/10.1016/0013-4694(58)90053-1.
5. Kolls, B.J., Lai, A.H., Srinivas, A.A., and Reid, R.R. (2014). Integration of EEG lead placement templates into traditional technologist-based staffing models reduces costs in continuous video-EEG monitoring service. J. Clin. Neurophysiol. *31*, 187–193. https://doi.org/10.1097/WNP.0000000000000053.
6. Kolls, B.J., Olson, D.M., Gallentine, W.B., Skeen, M.B., Skidmore, C.T., and Sinha, S.R. (2012). Electroencephalography leads placed by nontechnologists using a template system produce signals equal in quality to technologist-applied, collodion disk leads. J. Clin. Neurophysiol. *29*, 42–49. https://doi.org/10.1097/WNP.0b013e318246ae76.
7. Beam, W., Borckardt, J.J., Reeves, S.T., and George, M.S. (2009). An efficient and accurate new method for locating the f3 position for prefrontal tms applications. Brain Stimul. *2*, 50–54. https://doi.org/10.1016/j.brs.2008.09.006.
8. Li, J., Ma, Y., Huang, D., Wang, Z., Zhang, Z., Ren, Y., Hong, M., Chen, Y., Li, T., Shi, X., et al. (2022). High-performance flexible microneedle array as a low-impedance surface biopotential dry electrode for wearable electrophysiological recording and polysomnography. Nano Micro Lett. *14*, 132. https://doi.org/10.1007/s40820-022-00870-0.

9. Kennedy, J.D., and Gerard, E.E. (2012). Continuous EEG monitoring in the intensive care unit. Curr. Neurol. Neurosci. Rep. *12*, 419–428. https://doi.org/10.1007/s11910-012-0289-0.

10. Falco, C., Sebastiano, F., Cacciola, L., Orabona, F., Ponticelli, R., Stirpe, P., and Di Gennaro, G. (2005). Scalp electrode placement by EC2® adhesive paste in long-term video-EEG monitoring. Clin. Neurophysiol. *116*, 1771–1773. https://doi.org/10.1016/j.clinph.2005.04.012.

11. Kim, D.-H., Lu, N., Ma, R., Kim, Y.-S., Kim, R.-H., Wang, S., Wu, J., Won, S.M., Tao, H., Islam, A., et al. (2011). Epidermal electronics. Science *333*, 838–843. https://doi.org/10.1126/science.1206157.

12. Li, H., Tan, P., Rao, Y., Bhattacharya, S., Wang, Z., Kim, S., Gangopadhyay, S., Shi, H., Jankovic, M., Huh, H., et al. (2024). E-tattoos: Toward functional but imperceptible interfacing with human skin. Chem. Rev. *124*, 3220–3283. https://doi.org/10.1021/acs.chemrev.3c00626.

13. Ray, T.R., Choi, J., Bandodkar, A.J., Krishnan, S., Gutruf, P., Tian, L., Ghaffari, R., and Rogers, J.A. (2019). Bio-integrated wearable systems: a comprehensive review. Chem. Rev. *119*, 5461–5533. https://doi.org/10.1021/acs.chemrev.8b00573.

14. Sunwoo, S.-H., Ha, K.-H., Lee, S., Lu, N., and Kim, D.-H. (2021). Wearable and implantable soft bioelectronics: device designs and material strategies. Annu. Rev. Chem. Biomol. Eng. *12*, 359–391. https://doi.org/10.1146/annurev-chembioeng-101420-024336.

15. Liu, S., Rao, Y., Jang, H., Tan, P., and Lu, N. (2022). Strategies for body-conformable electronics. Matter *5*, 1104–1136. https://doi.org/10.1016/j.matt.2022.02.006.

16. Luo, Y., Abidian, M.R., Ahn, J.-H., Akinwande, D., Andrews, A.M., Antonietti, M., Bao, Z., Berggren, M., Berkey, C.A., Bettinger, C.J., et al. (2023). Technology roadmap for flexible sensors. ACS Nano *17*, 5211–5295. https://doi.org/10.1021/acsnano.2c12606.

17. Tan, P., Tamma, S., Bhattacharya, S., Tunnell, J., and Lu, N. (2022). Wearable optical e-tattoo for deep neck hemodynamic monitoring. In 2022 IEEE/ACM Conference on Connected Health: Applications, Systems and Engineering Technologies (CHASE), pp. 118–122. https://doi.org/10.1145/3551455.3559604.

18. García-López, I., and Rodriguez-Villegas, E. (2020). Extracting the jugular venous pulse from anterior neck contact photoplethysmography. Sci. Rep. *10*, 3466. https://doi.org/10.1038/s41598-020-60317-7.

19. Zipp, P. (1982). Recommendations for the standardization of lead positions in surface electromyography. Eur. J. Appl. Physiol. Occup. Physiol. *50*, 41–54. https://doi.org/10.1007/BF00952243.

20. Ratti, E., Waninger, S., Berka, C., Ruffini, G., and Verma, A. (2017). Comparison of medical and consumer wireless EEG systems for use in clinical trials. Front. Hum. Neurosci. *11*, 398. https://doi.org/10.3389/fnhum.2017.00398.

21. Yin, J., Wang, S., Tat, T., and Chen, J. (2024). Motion artefact management for soft bioelectronics. Nat. Rev. Bioeng. *2*, 541–558. https://doi.org/10.1038/s44222-024-00175-4.

22. Tian, L., Zimmerman, B., Akhtar, A., Yu, K.J., Moore, M., Wu, J., Larsen, R.J., Lee, J.W., Li, J., Liu, Y., et al. (2019). Large-area mri-compatible epidermal electronic interfaces for prosthetic control and cognitive monitoring. Nat. Biomed. Eng. *3*, 194–205. https://doi.org/10.1038/s41551-019-0347-x.

23. Hure, J., Roman, B., and Bico, J. (2011). Wrapping an adhesive sphere with an elastic sheet. Phys. Rev. Lett. *106*, 174301. https://doi.org/10.1103/PhysRevLett.106.174301.

24. Liu, S., He, J., Rao, Y., Dai, Z., Ye, H., Tanir, J.C., Li, Y., and Lu, N. (2023). Conformability of flexible sheets on spherical surfaces. Sci. Adv. *9*, eadf2709. https://doi.org/10.1126/sciadv.adf2709.

25. Wang, Y., Yin, L., Bai, Y., Liu, S., Wang, L., Zhou, Y., Hou, C., Yang, Z., Wu, H., Ma, J., et al. (2020). Electrically compensated, tattoo-like electrodes for epidermal electrophysiology at scale. Sci. Adv. *6*, 0996. https://doi.org/10.1126/sciadv.abd0996.

26. Ershad, F., Houston, M., Patel, S., Contreras, L., Koirala, B., Lu, Y., Rao, Z., Liu, Y., Dias, N., Haces-Garcia, A., et al. (2023). Customizable, reconfigurable, and anatomically coordinated large-area, high-density electromyography from drawn-on-skin electrode arrays. PNAS Nexus *2*, pgac291. https://doi.org/10.1093/pnasnexus/pgac291.

27. Kayser, L.V., and Lipomi, D.J. (2019). Stretchable conductive polymers and composites based on pedot and pedot:pss. Adv. Mater. *31*, e1806133. https://doi.org/10.1002/adma.201806133.

28. He, H., Zhang, L., Guan, X., Cheng, H., Liu, X., Yu, S., Wei, J., and Ouyang, J. (2019). Biocompatible conductive polymers with high conductivity and high stretchability. ACS Appl. Mater. Interfaces *11*, 26185–26193. https://doi.org/10.1021/acsami.9b07325.

29. Zhang, L., Kumar, K.S., He, H., Cai, C.J., He, X., Gao, H., Yue, S., Li, C., Seet, R.C.S., Ren, H., and Ouyang, J. (2020). Fully organic compliant dry electrodes self-adhesive to skin for long-term motion-robust epidermal biopotential monitoring. Nat. Commun. *11*, 4683. https://doi.org/10.1038/s41467-020-18503-8.

30. Zhang, S., Chen, Y., Liu, H., Wang, Z., Ling, H., Wang, C., Ni, J., Çelebi-Saltik, B., Wang, X., Meng, X., et al. (2020). Room-temperature-formed pedot:pss hydrogels enable injectable, soft, and healable organic bioelectronics. Adv. Mater. *32*, e1904752. https://doi.org/10.1002/adma.201904752.

31. Zhu, Z., Guo, S.-Z., Hirdler, T., Eide, C., Fan, X., Tolar, J., and McAlpine, M.C. (2018). 3D printed functional and biological materials on moving free-form surfaces. Adv. Mater. *30*, e1707495. https://doi.org/10.1002/adma.201707495.

32. Zhao, W., Chen, H., Zhang, Y., Zhou, D., Liang, L., Liu, B., and Xu, T. (2022). Adaptive multi-degree-of-freedom in situ bioprinting robot for hair-follicle-inclusive skin repair: A preliminary study conducted in mice. Bioeng. Transl. Med. *7*, e10303. https://doi.org/10.1002/btm2.10303.

33. Kucukdeger, E., and Johnson, B.N. (2023). Closed-loop controlled conformal 3D printing on moving objects via tool-localized object position sensing. J. Manuf. Process *89*, 39–49. https://doi.org/10.1016/j.jmapro.2023.01.020.

34. Choi, Y., Ryu, N., Kim, M.J., Dementyev, A., and Bianchi, A. (2020). Bodyprinter: Fabricating circuits directly on the skin at arbitrary locations using a wearable compact plotter. In Proceedings of the 33rd Annual ACM Symposium on User Interface Software and Technology, pp. 554–564. https://doi.org/10.1145/3379337.3415840.

35. Zhu, Z., Park, H.S., and McAlpine, M.C. (2020). 3D printed deformable sensors. Sci. Adv. *6*, eaba5575. https://doi.org/10.1126/sciadv.aba5575.

36. Park, J.-U., Hardy, M., Kang, S.J., Barton, K., Adair, K., Mukhopadhyay, D.K., Lee, C.Y., Strano, M.S., Alleyne, A.G., Georgiadis, J.G., et al. (2007). High-resolution electrohydrodynamic jet printing. Nat. Mater. *6*, 782–789. https://doi.org/10.1038/nmat1974.

37. Lin, L., Dautta, M., Hajiaghajani, A., Escobar, A.R., Tseng, P., and Khine, M. (2021). Paint-on epidermal electronics for on-demand sensors and circuits. Adv. Electron. Mater. *7*, 2000765. https://doi.org/10.1002/aelm.202000765.

38. Williams, N.X., Noyce, S., Cardenas, J.A., Catenacci, M., Wiley, B.J., and Franklin, A.D. (2019). Silver nanowire inks for direct-write electronic tattoo applications. Nanoscale *11*, 14294–14302. https://doi.org/10.1039/C9NR03378E.

39. Zhang, L., Ji, H., Huang, H., Yi, N., Shi, X., Xie, S., Li, Y., Ye, Z., Feng, P., Lin, T., et al. (2020). Wearable circuits sintered at room temperature directly on the skin surface for health monitoring. ACS Appl. Mater. Interfaces *12*, 45504–45515. https://doi.org/10.1021/acsami.0c11479.

40. Ershad, F., Thukral, A., Yue, J., Comeaux, P., Lu, Y., Shim, H., Sim, K., Kim, N.-I., Rao, Z., Guevara, R., et al. (2020). Ultra-conformal drawn-on-skin electronics for multifunctional motion artifact-free sensing and point-of-care treatment. Nat. Commun. *11*, 3823. https://doi.org/10.1038/s41467-020-17619-1.

41. Falland-Cheung, L., Scholze, M., Lozano, P.F., Ondruschka, B., Tong, D.C., Brunton, P.A., Waddell, J.N., and Hammer, N. (2018). Mechanical properties of the human scalp in tension. J. Mech. Behav. Biomed. Mater. *84*, 188–197. https://doi.org/10.1016/j.jmbbm.2018.05.024.

42. Huang, Q., and Zheng, Z. (2022). Pathway to developing permeable electronics. ACS Nano *16*, 15537–15544. https://doi.org/10.1021/acsnano.2c08091.

43. Ferree, T.C., Luu, P., Russell, G.S., and Tucker, D.M. (2001). Scalp electrode impedance, infection risk, and EEG data quality. Clin. Neurophysiol. *112*, 536–544. https://doi.org/10.1016/S1388-2457(00)00533-2.

44. Mantione, D., Del Agua, I., Sanchez-Sanchez, A., and Mecerreyes, D. (2017). Poly(3,4-ethylenedioxythiophene) (pedot) derivatives: Innovative conductive polymers for bioelectronics. Polymers *9*, 354. https://doi.org/10.3390/polym9080354.

45. Yuk, H., Lu, B., Lin, S., Qu, K., Xu, J., Luo, J., and Zhao, X. (2020). 3D printing of conducting polymers. Nat. Commun. *11*, 1604. https://doi.org/10.1038/s41467-020-15316-7.

46. Liu, Y., Liu, J., Chen, S., Lei, T., Kim, Y., Niu, S., Wang, H., Wang, X., Foudeh, A.M., Tok, J.B.-H., and Bao, Z. (2019). Soft and elastic hydrogel-based microelectronics for localized low-voltage neuromodulation. Nat. Biomed. Eng. *3*, 58–68. https://doi.org/10.1038/s41551-018-0335-6.

47. Murray, K.A., and Gibson, M.I. (2022). Chemical approaches to cryopreservation. Nat. Rev. Chem. *6*, 579–593. https://doi.org/10.1038/s41570-022-00407-4.

48. Lu, B., Yuk, H., Lin, S., Jian, N., Qu, K., Xu, J., and Zhao, X. (2019). Pure pedot:pss hydrogels. Nat. Commun. *10*, 1043. https://doi.org/10.1038/s41467-019-09003-5.

49. Fluhr, J.W., Darlenski, R., and Surber, C. (2008). Glycerol and the skin: holistic approach to its origin and functions. Br. J. Dermatol. *159*, 23–34. https://doi.org/10.1111/j.1365-2133.2008.08643.x.

50. Liu, Y., Li, J., Song, S., Kang, J., Tsao, Y., Chen, S., Mottini, V., McConnell, K., Xu, W., Zheng, Y.-Q., et al. (2020). Morphing electronics enable neuromodulation in growing tissue. Nat. Biotechnol. *38*, 1031–1036. https://doi.org/10.1038/s41587-020-0495-2.

51. Shi, H., Liu, C., Jiang, Q., and Xu, J. (2015). Effective approaches to improve the electrical conductivity of pedot:pss: A review. Adv. Electron. Mater. *1*, 1500017. https://doi.org/10.1002/aelm.201500017.

52. Ma, Z., Huang, Q., Xu, Q., Zhuang, Q., Zhao, X., Yang, Y., Qiu, H., Yang, Z., Wang, C., Chai, Y., and Zheng, Z. (2021). Permeable superelastic liquid-metal fibre mat enables biocompatible and monolithic stretchable electronics. Nat. Mater. *20*, 859–868. https://doi.org/10.1038/s41563-020-00902-3.

53. Yoon, S., Seok, M., Kim, M., and Cho, Y.-H. (2021). Wearable porous pdms layer of high moisture permeability for skin trouble reduction. Sci. Rep. *11*, 938. https://doi.org/10.1038/s41598-020-78580-z.

54. Webster, J.G. (2006). Encyclopedia of Medical Devices and Instrumentation (John Wiley & Sons, Inc.).

55. He, H., Chen, R., Yue, S., Yu, S., Wei, J., and Ouyang, J. (2022). Salt-induced ductilization and strain-insensitive resistance of an intrinsically conducting polymer. Sci. Adv. *8*, eabq8160. https://doi.org/10.1126/sciadv.abq8160.

56. Jung, S., and Hutchings, I.M. (2012). The impact and spreading of a small liquid drop on a non-porous substrate over an extended time scale. Soft Matter *8*, 2686–2696. https://doi.org/10.1039/C2SM06565G.

57. Bießmann, L., Kreuzer, L.P., Widmann, T., Hohn, N., Moulin, J.-F., and Müller-Buschbaum, P. (2018). Monitoring the Swelling Behavior of PEDOT:PSS Electrodes under High Humidity Conditions. ACS Appl. Mater. Interfaces *10*, 9865–9872. https://doi.org/10.1021/acsami.8b00446.

58. Dalal, S.S., Rampp, S., Willomitzer, F., and Ettl, S. (2014). Consequences of EEG electrode position error on ultimate beamformer source reconstruction performance. Front. Neurosci. *8*, 80684. https://doi.org/10.3389/fnins.2014.00042.

59. Giacometti, P., Perdue, K.L., and Diamond, S.G. (2014). Algorithm to find high density EEG scalp coordinates and analysis of their correspondence to structural and functional regions of the brain. J. Neurosci. Methods *229*, 84–96. https://doi.org/10.1016/j.jneumeth.2014.04.020.

60. Herman, S.T., Abend, N.S., Bleck, T.P., Chapman, K.E., Drislane, F.W., Emerson, R.G., Gerard, E.E., Hahn, C.D., Husain, A.M., Kaplan, P.W., et al. (2015). Consensus statement on continuous EEG in critically ill adults and children, part ii: personnel, technical specifications, and clinical practice. J. Clin. Neurophysiol. *32*, 96–108. https://doi.org/10.1097/WNP.0000000000000165.

61. Dai, H., Pears, N., Smith, W., and Duncan, C. (2020). Statistical modeling of craniofacial shape and texture. Int. J. Comput. Vision *128*, 547–571. https://doi.org/10.1007/s11263-019-01260-7.

62. Park, B.D., Corner, B.D., Hudson, J.A., Whitestone, J., Mullenger, C.R., and Reed, M.P. (2021). A three-dimensional parametric adult head model with representation of scalp shape variability under hair. Appl. Ergon. *90*, 103239. https://doi.org/10.1016/j.apergo.2020.103239.

63. Burbank, D.P., and Webster, J.G. (1978). Reducing skin potential motion artefact by skin abrasion. Med. Biol. Eng. Comput. *16*, 31–38. https://doi.org/10.1007/BF02442929.

64. Kappenman, E.S., and Luck, S.J. (2010). The effects of electrode impedance on data quality and statistical significance in erp recordings. Psychophysiology *47*, 888–904. https://doi.org/10.1111/j.1469-8986.2010.01009.x.

65. Kumar, S., Alawieh, H., Racz, F.S., Fakhreddine, R., and Millán, J.D.R. (2024). Transfer learning promotes acquisition of individual BCI skills. PNAS Nexus *3*, pgae076. https://doi.org/10.1093/pnasnexus/pgae076.

66. Alawieh, H., Liu, D., Madera, J., Kumar, S., Racz, F.S., Majewicz Fey, A., and Millán, J.d.R. (2024). Transcutaneous electrical spinal cord stimulation promotes focal sensorimotor activation that accelerates brain-computer interface skill learning. Preprint at medRxiv.

67. Chavarriaga, R., Sobolewski, A., and Millán, J.d.R. (2014). Errare machinale est: the use of error-related potentials in brain-machine interfaces. Front. Neurosci. *8*, 86996. https://doi.org/10.3389/fnins.2014.00208.

68. Iwane, F., Iturrate, I., Chavarriaga, R., and Millán, J.D.R. (2021). Invariability of EEG error-related potentials during continuous feedback protocols elicited by erroneous actions at predicted or unpredicted states. J. Neural Eng. *18*, 888046044. https://doi.org/10.1088/1741-2552/abfa70.

69. Choy, T., Baker, E., and Stavropoulos, K. (2022). Systemic racism in EEG research: considerations and potential solutions. Affect. Sci. *3*, 14–20. https://doi.org/10.1007/s42761-021-00050-0.

70. Webb, E.K., Etter, J.A., and Kwasa, J.A. (2022). Addressing racial and phenotypic bias in human neuroscience methods. Nat. Neurosci. *25*, 410–414. https://doi.org/10.1038/s41593-022-01046-0.

71. Etienne, A., Laroia, T., Weigle, H., Afelin, A., Kelly, S.K., Krishnan, A., and Grover, P. (2020). Novel electrodes for reliable EEG recordings on coarse and curly hair. In Annu. Int. Conf. IEEE Eng. Med. Biol. Soc. 42nd Annual International Conference of the IEEE Engineering in Medicine & Biology Society (EMBC) (IEEE Publications), pp. 6151–6154. https://doi.org/10.1109/EMBC44109.2020.9176067.

72. Li, H., Shin, H., Sentis, L., Siu, K.-C., Millán, J.d.R., and Lu, N. (2024). Combining VRhigh with electroencephalography as a frontier of brain-computer interfaces. Device *2*, 100425. https://doi.org/10.1016/j.device.2024.100425.

73. Park, Y.-G., Yun, I., Chung, W.G., Park, W., Lee, D.H., and Park, J.-U. (2022). High-resolution 3D printing for electronics. Adv. *9*, e2104623. https://doi.org/10.1002/advs.202104623.

74. Park, Y.-G., Kwon, Y.W., Koh, C.S., Kim, E., Lee, D.H., Kim, S., Mun, J., Hong, Y.-M., Lee, S., Kim, J.-Y., et al. (2024). In-vivo integration of soft neural probes through high-resolution printing of liquid electronics on the cranium. Nat. Commun. *15*, 1772. https://doi.org/10.1038/s41467-024-45768-0.

75. Li, N., Li, Y., Cheng, Z., Liu, Y., Dai, Y., Kang, S., Li, S., Shan, N., Wai, S., Ziaja, A., et al. (2023). Bioadhesive polymer semiconductors and

transistors for intimate biointerfaces. Science *381*, 686–693. https://doi.org/10.1126/science.adg8758.

76. Cao, Y., Tan, J., Zhao, H., Deng, T., Hu, Y., Zeng, J., Li, J., Cheng, Y., Tang, J., Hu, Z., et al. (2022). Bead-jet printing enabled sparse mesenchymal stem cell patterning augments skeletal muscle and hair follicle regeneration. Nat. Commun. *13*, 7463. https://doi.org/10.1038/s41467-022-35183-8.

77. Li, L., Yu, F., Shi, J., Shen, S., Teng, H., Yang, J., Wang, X., and Jiang, Q. (2017). In situ repair of bone and cartilage defects using 3D scanning and 3D printing. Sci. Rep. *7*, 9416. https://doi.org/10.1038/s41598-017-10060-3.

78. Kérourédan, O., Hakobyan, D., Rémy, M., Ziane, S., Dusserre, N., Fricain, J.-C., Delmond, S., Thébaud, N.B., and Devillard, R. (2019). In situ prevascularization designed by laser-assisted bioprinting: effect on bone regeneration. Biofabrication *11*, 045002. https://doi.org/10.1088/1758-5090/ab2620.

79. Barone, D.G., and Malliaras, G.G. (2019). Epidermal electrophysiology at scale. Nat. Biomed. Eng. *3*, 165–166. https://doi.org/10.1038/s41551-019-0365-8.

80. Kwon, Y.W., Ahn, D.B., Park, Y.-G., Kim, E., Lee, D.H., Kim, S.-W., Lee, K.-H., Kim, W.-Y., Hong, Y.-M., Koh, C.S., et al. (2024). Power-integrated, wireless neural recording systems on the cranium using a direct printing method for deep-brain analysis. Sci. Adv. *10*, eadn3784. https://doi.org/10.1126/sciadv.adn3784.

81. Wang, L., and Lu, N. (2016). Conformability of a Thin Elastic Membrane Laminated on a Soft Substrate With Slightly Wavy Surface. J. Appl. Mech. *83*, 041007. https://doi.org/10.1115/1.4032466.

82. Oostenveld, R., and Praamstra, P. (2001). The five percent electrode system for high-resolution EEG and ERP measurements. Clin. Neurophysiol. *112*, 713–719. https://doi.org/10.1016/S1388-2457(00)00527-7.

83. Perdikis, S., Tonin, L., Saeedi, S., Schneider, C., and Millán, J.D.R. (2018). The Cybathlon BCI race: Successful longitudinal mutual learning with two tetraplegic users. PLOS Biol. *16*, e2003787. https://doi.org/10.1371/journal.pbio.2003787.

84. Leeb, R., Perdikis, S., Tonin, L., Biasiucci, A., Tavella, M., Creatura, M., Molina, A., Al-Khodairy, A., Carlson, T., and Millán, J.D.R. (2013). Transferring brain-computer interfaces beyond the laboratory: Successful application control for motor-disabled users. Artif. Intell. Med. *59*, 121–132. https://doi.org/10.1016/j.artmed.2013.08.004.

85. Barachant, A., Bonnet, S., Congedo, M., and Jutten, C. (2012). Multiclass brain-computer interface classification by Riemannian geometry. IEEE Trans. Bio Med. Eng. *59*, 920–928. https://doi.org/10.1109/TBME.2011.2172210.

86. Yger, F., Berar, M., and Lotte, F. (2017). Riemannian approaches in brain-computer interfaces: A review. IEEE Trans. Neural Syst. Rehabil. Eng. *25*, 1753–1762. https://doi.org/10.1109/TNSRE.2016.2627016.

CELBIO, Volume *1*

Supplemental information

On-scalp printing of personalized electroencephalography e-tattoos

Luize Scalco de Vasconcelos, Yichen Yan, Pukar Maharjan, Satyam Kumar, Minsu Zhang, Bowen Yao, Hongbian Li, Sidi Duan, Eric Li, Eric Williams, Sandhya Tiku, Pablo Vidal, R. Sergio Solorzano-Vargas, Wen Hong, Yingjie Du, Zixiao Liu, Fumiaki Iwane, Charles Block, Andrew T. Repetski, Philip Tan, Pulin Wang, Martín G. Martín, José del R. Millán, Ximin He, and Nanshu Lu

Supplemental Notes

Note S1: Significance to the diagnosis of epilepsy and other neurological conditions

Epileptic seizures are repetitive, unpredictable, and short-lasting neurological disorders that disrupt a person's life and are associated with significant morbidity and mortality.[1] Next to migraine, stroke, and Alzheimer's disease, epilepsy is the fourth most common neurological problem.[2] Because they are unpredictable and life-threatening, objective seizure monitoring through video-electroencephalography (VEEG) in the epilepsy monitoring unit (EMU) is a well-established gold standard for epilepsy evaluation.[3,4] However, VEEG requires stays in epilepsy monitoring units (EMUs) that are expensive and unavailable in many parts of the world. Routine EEG is done with a minimum of 16 channels for 30 to 60 minutes.[5] Various stimuli are provided at this time to improve the chances of yielding significant data. Still, this procedure can detect seizures for only 50% of cases.[5] Alternative methods, such as mobile, long-term EEG[6] are readily available and can be taken home. Recording EEG for extended periods can detect seizures in the majority of cases (80-100%)[7] and allows practitioners to get data from settings that routine EEG cannot replicate, such as under a normal stress environment and during sleep and wakening.[8,9] It can also be used to monitor medication effects.[4,5] Current EEG sensors are bulky and difficult to hide, meaning users often have to avoid certain aspects of life for fear of potential embarrassment. The obstructive and stigmatizing nature of current EEG technology can discourage patients from carrying out routine activities, hindering diagnosis under normal conditions and inhibiting the willingness to participate in EEG.[10,11] In addition, it requires electrode maintenance, often twice daily by trained personnel.[7] Because of these practical constraints, most outpatients still document seizure occurrence manually without EEG, which results in 50% underreporting compared to objective evaluations using VEEG.[3] Thus, there is currently a significant gap for a technology that overcomes the need for EMUs and is not associated with significant discomfort and societal stigma.

Note S2: Jet dispensing ink requirements

Our jetting tool is a drop-on-demand non-contact ink dispensing that utilizes a high-precision microdispensing valve with a shockwave-induced actuator (MDV 2560, VERMES Microdispensing GmbH). This tool uses needle-collision type actuation in which the cartridge pressure drives the fluid into the nozzle and the actuator pressure pulse drives the needle to open and close the nozzle. Piezo-, instead of air pressure-actuated needle-collision jetting is also common.[12] The needle collision-type actuators enable greater versatility to work with low- to high-viscosity materials and generally impose much less stringent requirements on the ink properties than the bend-type actuation typically used in inkjet printers such as the Dimatix and HP Deskjet. The main difference is scale. In bend-type actuation, the printhead typically has

multiple nozzles, which dispense pL volume drops of liquids with viscosity ranging from 1 cP to 20 cP, at frequencies up to 20 kHz, enabling printing feature sizes down to 20 µm. In needle-type jetting, the printhead has a single nozzle, which dispenses nL volume drops of fluids or pastes with viscosity up to 2,000,000 cP at maximum frequencies in the order of 100 to 3000 Hz, resulting in lower resolution (minimum feature size of 100 µm).[12–14]

It is worth noting that bend-type jetting, and other similar high-resolution jetting mechanisms, are widely known as inkjet.[12] The terminology for needle-type jetting is less well-defined. The industry manufacturers of these tools generally differentiate them from typical inkjet as simply jet dispensing or microjet,[14] however, they are also confounded as inkjet in the general literature.[12] For explicitness, we use the microjet terminology in this work. A comparison between microjet and other ink dispensing techniques is shown in Table S3. Microjet dispensing is less prone to the typical issues of high-resolution inkjet such as nozzle clogging and jet misfiring and the associated ink requirements (low evaporation rate, finely controlled particle suspension, surface tension and viscosity, and thorough filtering and degassing).[15] Our PEDOT:PSS inks displayed viscosity well within the suitable range for microjetting with favorable shear thinning behavior (Figure S11). The electrode ink had lower viscosity than the interconnect ink. This may be linked to the fact that DMSO (only present in the interconnect ink) causes PEDOT:PSS colloidal particles to change from coil to fibril structure which enhances the interaction between them. Also, salt ions in the electrode ink may cause a reduction in the electrostatic repulsions among the colloidal particles, leading to a decrease in viscosity.

Another ink dispensing option was extrusion printing. This technique is ideal for building 3D structures layer-by-layer, however, we argue that microjetting is a more suitable approach for in-situ digital printing of epidermal electronics, especially on highly curved and hairy body parts. Extrusion printing, also known simply as 3D printing or contact printing, requires a tight control of the nozzle and substrate distance. This distance is usually in order of the thickness of the ink trace being deposited. In contrast, microjetting can be dispensed across distances larger than 1 cm and can tolerate fluctuations in this distance without disrupting the ink trace. At the same time, the ability to dispense drops on demand and at high speeds is crucial for the ink to reach the scalp, passing through hair obstructions. In extrusion printing, one continuous trace is dispensed, which does not carry significant inertia, being more easily blocked and pulled by randomly oriented hairs along the way.

Note S3: Noise in EEG recording

Scalp EEG is measured using differential amplifiers, where the potential of both recording and reference electrodes are measured relative to a common electrode and only the difference in the potential is amplified. This approach rejects common noise, including electrocardiogram (ECG) and electromyography (EMG) signals, as well as power line noise. The electric potentials right

beneath the skin-electrode interface may differ from those recorded by the amplifier due to the influence of external electromagnetic fields interacting with the electrode leads and the body, motion artifacts, and current flowing into the amplifier. The electrical current flowing through the leads into the amplifier would cause signal attenuation, however, in modern devices, this attenuation is negligible ($< 0.025\%$) thanks to the high input impedance of the amplifier (~ 200 MΩ) relative to that of the electrode (typically < 50 kΩ).[16] The electromagnetic interference (60 Hz noise) from power lines can be rejected if the mismatch impedance between electrodes is sufficiently small. Other significant noise sources are motion artifacts and skin potentials. For conventional electrodes made of metal disks interfacing the skin through electrolytic gels, motion artifacts can be especially problematic if the metal is polarizable, such that when the gel is disturbed, or there is relative movement, the half-cell potential varies as a result of the variation in the metallic ion gradient at the interface. If non-polarizable electrodes such as silver chloride are used, the artifact from electrode movement is less significant as long as the contact with the gel is not completely disrupted.[17]

Ultimately, minimizing the electrode skin-interface impedance translates into a higher common mode rejection ratio and fewer artifacts, maximizing the EEG signal-to-noise ratio. The maximum acceptable threshold depends on the application. For example, consistently achieving impedance < 20 kΩ requires abrasion, which adds to the preparation time and can cause bleeding, becoming challenging or impractical for high-density EEG (hundreds of electrodes) and pediatric patients. Also, the benefit of lowering the impedance below 50 kΩ depends largely on the environment, type of analysis (event-related vs frequency domain), and whether pre-amplification is used.[18] In general, 40 kΩ (at 10 Hz) provides sufficient common-noise rejection.[16]

Note S4: Low contact impedance electrode properties

We tested different strategies to lower the skin-electrode interface impedance (Figure S8a). In this discussion, unless noted, the term skin-electrode impedance will imply specific skin-electrode impedance (i.e., impedance multiplied by the projected electrode area) at 10 Hz. The first strategy is conformal contact. Rigid and comb-type dry electrodes have a high impedance, over several hundred kΩ, due to the limited contact points with the rugged skin topography.[19] In comparison, we test a more dilute version of the silver ink developed by Zhu et al.[20] (silver flakes and polyethylene oxide in a dual solvent system comprised of water and ethanol). This ink forms a seemly conformal contact with the skin (Figure S8b), enabling a specific skin-electrode impedance below 400 kΩ (Figure S8c - green square symbols). Another factor is skin hydration. The outermost layer of the skin, the stratum corneum, is the dominant component of skin impedance, and moisturizers are known to increase the permeability to current-carrying ions within this layer, reducing impedance.[21,22] This effect can be seen by the reduced

impedance (in the range of $100 \sim 200$ kΩ) of a commercial, salt-free moisturizing wet gel (Spectra 360, gray hollow circles in Figure S8c) as well as a water-based commercial carbon ink containing humectants (Bare ink, red hollow circles). The saline-free version of our water-based PEDOT:PSS electrode ink also achieves impedance in this range (blue hollow circles), which may be attributed to the glycerol's moisturizing effect.

To further reduce the impedance, it is necessary to increase the ion concentration on the electrode interface with the stratum corneum.[23] For example, the commercial saline wet gel (Signal Gel, grey-filled circles) and our saline PEDOT:PSS electrode ink (blue-filled circles) both achieve impedance under 50 kΩ. It is important to note that many of these strategies are targeted at counteracting the high impedance of the stratum corneum, which can be bypassed by mechanical skin abrasion.[24] Thus, virtually any conductive material can offer low impedance if the stratum corneum is abraded. To demonstrate this, we repeat the measurement using the commercial carbon ink. The same ink has an impedance > 100 kΩ on natural skin (red empty circles) and < 5 kΩ if the skin is abraded before the ink application (red triangles). We, therefore, emphasize that comparisons of the effectiveness of different electrode materials are only relevant if the surface conditions are equivalent. That means maintaining every preparation step identical, including how the skin is cleaned and degreased, the region of the body being measured, and ideally using the same subject or a sufficient sample size since age and individual skin characteristics can also bias the measurement.

Note S5: Ink property requirements for EEG electrodes and interconnects

Interconnect electrical conductivity. The interconnect ink bulk conductivity requirement depends on the dimensions of the interconnect trace and the acceptable end-to-end resistance of the interconnect. For the interconnect to have a minor contribution to the total channel impedance (i.e., interconnect plus skin-electrode components) of roughly 6% assuming that the electrode impedance is 40 kΩ (recommended threshold as discussed in Note S3), the maximum interconnect resistance would be $R_{max} = 2.5$ kΩ. For our interconnect thickness, h, in the range of 20 to 30 µm, width, w, of ∼2 mm, and a maximum interconnect length, l_{max}, of 50 cm, the minimum acceptable bulk conductivity is $\sigma_{min} = (l_{max})/(whR_{max}) = 40$ S/cm. This criterion is satisfied by our interconnect ink conductivity of 83 S/cm. The resistances of the on-scalp printed interconnects routing channels C5, P5, FCC1h, Cz, Pz, P4, C4, and C6 (Figure S21a) were measured with a multimeter (Figure S21c) right after drying (0h) and after 6h. The average interconnect resistance was 1.457 kΩ at 0h and 1.451 kΩ at 6h, and the maximum interconnect resistance was 1.95 kΩ, which are in the expected range.

Electrode-skin specific impedance. The electrode impedance is proportional to the specific impedance (kΩ·cm^2) and the electrode area (cm^2). Too large an area will sacrifice resolution and limit the number of channels

that can be accommodated. Based on the specific impedance measured on the forehead (Figure 4a and Figure S9), a circular electrode with a 1.55 cm diameter should exhibit impedance $12 \sim 17$ kΩ (including the interconnect resistance contribution), however, the effective on-scalp printed electrode impedance was somewhat higher at 24 kΩ (average across 10 head locations and 5 subjects, Figure 4a). We attribute the deviation largely to the intrinsic difference between the forehead and scalp impedance. Albeit often overlooked, the dependence of the skin impedance on the body region is not surprising.[25] The lower impedance on the forehead compared to the scalp agrees with previous studies.[26] This was attributed to the thinner stratum corneum on the face and the higher density of sweat glands. Other factors, such as the hindered ability to effectively clean multiple sites on the hairy scalp, as well as subject-to-subject variation, may also have contributed to this difference.

Mechanical compliance. For the on-skin printed film not to delaminate or crack under buckling or bending of the skin, and to be physically imperceptible to the user, the mechanical compliance should be as high as possible. High mechanical compliance is achieved by minimizing elastic modulus and thickness. Typically, there is a trade-off between elastic modulus and electrical conductivity.[27] For the PEDOT:PSS ink, the proportions of the additives were tuned to achieve the lowest modulus while still meeting the electrical conductivity requirement of > 40 S/cm. The thickness of the printed film depends on the microjet settings (frequency, nozzle open/closed duration, and cartridge pressure) relative to nozzle translation speed and the substrate surface properties. The maximum nozzle travel speed of 200 mm/min was selected for safety to allow sufficient reaction time for emergency stops. The jetting parameters were tuned by trial and error to achieve the thinnest possible film while still allowing sufficient leeway for head movement and jet misfiring to take place without disrupting the conductive trace. To measure the thickness of the electrode and interconnect films printed on the skin using this optimized configuration, the dry film was peeled off from the skin and probed with a micrometer, standing at roughly 30 µm. This value was similar to that of a film printed on PDMS using the same printer configuration and subsequently measured by atomic force microscopy (Figure S14). The conformability can be estimated according to the method reported here by Wang and Lu[28]. As highlighted by the red dots in Figure S27, the global energy minimum for the printed electrode and interconnect falls at $\hat{x}_c = 1$, indicating that the printed e-tattoo fully conforms to the scalp surface, completely following its surface morphology without any interfacial gap. In contrast, the global energy minimum for the transferred electrode and interconnect falls at $\hat{x}_c = 0.21$, suggesting that the transferred e-tattoo only partially conforms to the scalp surface, leaving a large interfacial gap. Therefore, our on-scalp printed e-tattoo demonstrates improved conformability with the human scalp compared to conventional transferred e-tattoo. The calculation parameters are detailed

as follows. Except for the adhesion strength, the same dimensions and properties are used for the printed-on and transferred e-tattoos. The thickness is *t* = 30 μm, and the moduli of the electrode and interconnect are $E_e = 28$ MPa and E_i = 66 MPa, respectively. The undeformed scalp has a semi-amplitude of h_0 = 40 μm and a wavelength of λ = 250 μm. The modulus of the scalp is E_s = 92 kPa. The interface work of adhesion was taken from the peel test experiments in Figure 1h. For the printed-on electrode and interconnect, as well as for the transferred electrode and interconnect, the works of adhesion are γ_{pe} = 15 N/m, γ_{pi} = 18 N/m, and $\gamma_{te} = \gamma_{ti}$ = 0.4 N/m, respectively.

Note S6: Algorithm to generate the custom electrode-interconnect layout and the 5-axis printer control instructions

The personalized electrode and interconnect layout design was automated using a MATLAB script. The 3D model of the user's head is in triangular mesh format (STL format), consisting of N mesh elements, each having a corresponding normal vector $\hat{\mathbf{n}}_i$:

$$\hat{\mathbf{n}}_i = [x_i, y_i, z_i], i \in 1...N.$$

Four fiducials in the head anatomy are used as reference points: nasion (the indentation between the forehead and the nose), inion (the ridge between the neck and skull), and left and right pre-auricular points (indentations above the cartilage that covers the external ear opening). In the current script, the coordinates of these four points ($\mathbf{p_{nasion}}$, $\mathbf{p_{inion}}$, $\mathbf{p_{left}}$ and $\mathbf{p_{right}}$) are manually defined; however, this step could also be automated, for example, by integrating the machine learning-based fiducial detection function by Martínez et al.[29]. The origin is set at the nasion such that $\mathbf{p_{nasion}} = [0, 0, 0]$ and the midpoint between the pre-auricular points prescribe the positive x-direction and the xz-plane corresponds to the head symmetry plane. We use the opensource function by Giacometti et al.[30] to compute the electrode coordinates, $\mathbf{E}_j$, according to the 10-20 system[31] and its higher density derivatives (10-10 and 10-5 systems).[32] Here j is the electrode index, ranging from 1 to N_e (total number of electrodes). For the selected montage in Figure 5b, $N_e = 10$. Each electrode is routed to a terminal in the neck by finding the intercept between the head mesh and the plane defined by the electrode $\mathbf{E}_j$, the terminal $\mathbf{T}_j$, and an intermediate $\mathbf{I}_j$ reference points (Figure 3a). The set of terminal and intermediate reference points are each defined relative to the pre-auricular fiducial markers along a line perpendicular to the head symmetry plane. The neck terminal reference points, $\mathbf{T}_j \leftarrow [T_{j,x}, T_y, T_z]$, are distributed along a length corresponding to 70% the distance between pre-auricular points (ear-to-ear distance) as illustrated in Figure S18. That is, the x coordinate for the terminals connecting to the leftmost and rightmost electrodes are, respectively, $T_{1,x} \leftarrow -0.35(p_{left_x} - p_{right_x})$, and $T_{N_e,x} \leftarrow +0.35(p_{left_x} - p_{right_x})$. Similarly, the set of intermediate reference points $\mathbf{I}_j \leftarrow [I_{j,x}, I_y, I_z]$ span a length corresponding to 80% the ear-to-ear distance:

$I_{1,x} \leftarrow -0.4(p_{left_x} - p_{right_x})$ and $I_{N_e,x} \leftarrow +0.4(p_{left_x} - p_{right_x})$. For each electrode, j, the set of these three reference points ($\mathbf{E}_j$,$\mathbf{T}_j$,$\mathbf{I}_j$) define the equation of the interconnect plane $a_j x + b_j y + c_j z + d_j = 0$ and the interconnect plane normal vector $\mathbf{n}_{\mathbf{I}j} = [n_{Ij,x}, n_{Ij,y}, n_{Ij,z}]$, as follows:

$$\mathbf{n}_{\mathbf{I}j} \leftarrow (\mathbf{I}_j - \mathbf{E}_j) \times (\mathbf{T}_j - \mathbf{E}_j)$$
$$a_j \leftarrow n_{Ij,x}$$
$$b_j \leftarrow n_{Ij,y}$$
$$c_j \leftarrow n_{Ij,z}$$
$$d_j \leftarrow -(a_j E_{j,x} + b_j E_{j,y} + c_j E_{j,z}).$$

The algorithm then creates segments from the intersection points between the interconnect plane and all mesh elements, forming a continuous contour (slice, Figure 3a). To determine which mesh elements intercept the interconnect plane, the mesh elements with vertices on opposite sides (intercepting element) are kept, and elements with all three vertices on one side of the plane (non-intercepting elements) are discarded. Whether any point $\mathbf{p}$ lies on one side or the other of the plane is dictated by the sign of v:

$$v \leftarrow a_j p_x + b_j p_y + c_j p_z + d_j.$$

To generate the interconnect path j, the algorithm loops through all mesh elements having vertices on opposite sides of the plane (i.e., mesh elements with vertices with non-matching v signs). The intercept between the entire head mesh and interconnect plane consists of a conformal path passing through the terminal and the electrode, forming a closed loop around the head. To keep only the points between the terminal and electrode, a third plane parallel to the x-axis that contains both electrode and terminal is used as a partition to discard the outer points. As a result, for each j electrode, a matrix $\mathbf{It}_j$ of variable length contains the coordinates of a sequence of points defining the interconnect toolpath and the normal vectors of each corresponding mesh element. The normal vectors will be required later to plan the robot offsets and joint angles. Lastly, the script orders all points and smooths out the normal vectors along the interconnect path through a moving average.

Notably, the approach presented here to design the custom interconnects does not explicitly prevent interconnects from overlapping with themselves or the electrodes. Nevertheless, once the intermediate reference point coordinates are tuned for a specific montage, this approach generates ready-to-print layouts across different subjects. More complex montages would require a more advanced script to optimize the routing and explicitly prohibit overlapping.

The electrode toolpath generation is more straightforward due to its small size relative to the head curvature. A generic 2D design $\mathbf{Et}'$ (zigzag pattern) having a geometrical center at the local origin is used (blue line in the top-left corner graph, Figure 3a). The generic electrode toolpath is transformed

from the local coordinate system to the global coordinate system, using the electrode coordinates $\mathbf{E}_j$ and its normal vector $\hat{\mathbf{n}}_{\mathbf{E}_j}$ as follows:

$$\mathbf{Et}_j \leftarrow \mathbf{Et}' \cdot \left[\frac{\mathbf{x}'_j}{\|\mathbf{x}'_j\|}, \frac{\mathbf{y}'_j}{\|\mathbf{y}'_j\|}, \hat{\mathbf{z}}'_j \right] + \mathbf{E}_j$$

where $\mathbf{x}'_j \leftarrow \mathbf{p_a} - \mathbf{E}_j$ and $\mathbf{y}'_j \leftarrow \hat{\mathbf{n}}_{\mathbf{E}_j} \times \mathbf{x}'_j$, $\hat{\mathbf{z}}'_j \leftarrow \hat{\mathbf{n}}_{\mathbf{E}_j}$ and $\mathbf{p_a}$ is an arbitrary point within the plane mesh element plane (determines the direction of the local x-axis in the global reference frame).

Next, the custom electrode-interconnect layout is processed into control instructions for the printer. The first step is pose-matching the digital head model to the physical head's real time position and orientation in the printer coordinate system. This is implemented using the coordinates of three digital $\mathbf{F}_{\mathbf{d}k}$ and physical $\mathbf{F}_{\mathbf{p}k}$ fiducial landmarks where $k \in 1, 2, 3$ denotes the landmark index (Figure S19). Here, any arbitrary toolpath $\mathbf{P}$ defined in the head mesh global coordinate system is first mapped to the local coordinate system of the fiducials and subsequently mapped to the printer's global coordinate as $\mathbf{P}''$ as follows.

$$\hat{\mathbf{n}}_{\mathbf{p}} \leftarrow \frac{(\mathbf{F_{p2}} - \mathbf{F_{p1}}) \times (\mathbf{F_{p3}} - \mathbf{F_{p2}})}{\|(\mathbf{F_{p2}} - \mathbf{F_{p1}}) \times (\mathbf{F_{p3}} - \mathbf{F_{p2}})\|}$$

$$\hat{\mathbf{n}}_{\mathbf{d}} \leftarrow \frac{(\mathbf{F_{d2}} - \mathbf{F_{d1}}) \times (\mathbf{F_{d3}} - \mathbf{F_{d2}})}{\|(\mathbf{F_{d2}} - \mathbf{F_{d1}}) \times (\mathbf{F_{d3}} - \mathbf{F_{d2}})\|}$$

$$\hat{\mathbf{v}}_{\mathbf{d}} = \mathbf{F_{d2}} - \mathbf{F_{d1}}$$

$$\hat{\mathbf{v}}_{\mathbf{p}} = \mathbf{F_{p2}} - \mathbf{F_{p1}}$$

$$\mathbf{P}'' = (\mathbf{P} - \mathbf{F_{d1}}) \left[\hat{\mathbf{v}}_{\mathbf{d}}, \frac{\hat{\mathbf{n}}_{\mathbf{d}} \times \hat{\mathbf{v}}_{\mathbf{d}}}{\|\hat{\mathbf{n}}_{\mathbf{d}} \times \hat{\mathbf{v}}_{\mathbf{d}}\|}, \hat{\mathbf{v}}_{\mathbf{d}} \right]^{-1} \left[[\hat{\mathbf{v}}_{\mathbf{p}}, \frac{\hat{\mathbf{n}}_{\mathbf{p}} \times \hat{\mathbf{v}}_{\mathbf{p}}}{\|\hat{\mathbf{n}}_{\mathbf{p}} \times \hat{\mathbf{v}}_{\mathbf{p}}\|}, \hat{\mathbf{v}}_{\mathbf{p}}] \right] + \mathbf{F_{p1}}$$

Because precisely matching all three points is impossible due to real-world limited measurement precision (overconstrained problem), what this operation effectively does is to exactly match the digital and physical positions of the first fiducial point $\mathbf{F_{p1}}$ and $\mathbf{F_{d1}}$, the fiducial plane normal unit vectors $\hat{\mathbf{n}}_{\mathbf{p}}$ and $\hat{\mathbf{n}}_{\mathbf{d}}$, and the unit vectors connecting the fiducial points 1 and 2, $\hat{\mathbf{v}}_{\mathbf{p}}$ and $\hat{\mathbf{v}}_{\mathbf{d}}$, while allowing some offset between fiducial points $\mathbf{F_{p2}}$ and $\mathbf{F_{d2}}$, and $\mathbf{F_{p3}}$ and $\mathbf{F_{d3}}$. With this operation, the toolpath in the printer's coordinate system for the physical pose of the subject is obtained for the interconnects, $\mathbf{It}''_j$, and electrodes, $\mathbf{Et}''_j$, as well as their corresponding sets of normal vectors $\hat{\mathbf{n}}''_{\mathbf{It}_j}$ and $\hat{\mathbf{n}}''_{\mathbf{Et}_j}$.

Generating G-code for a 5-axis printer presents challenges compared to a 3-axis configuration due to the increased complexity of motion. The inverse kinematics problem of computing the joint angles required to achieve a desired end-effector position and orientation becomes more complex due to the additional degrees of freedom. Here, we need to determine the end-effector X, Y, Z, B, C coordinates for any given point $\mathbf{p} = [p_x, p_y, p_z]$ printed at a target surface with normal vector $\hat{\mathbf{n}} = [n_x, n_y, n_z]$. The C- and B-angles

correspond to the rotation of the effector along the vertical and horizontal axes (Figure 3). We define $C = 0$ when the B-axis is oriented in the x-axis direction and $B = 0$ when the jetting axis is vertical. For every point in space that maintains the jetting axis normal to the target surface, the inverse kinematic problem give infinite compatible poses when $\hat{\mathbf{n}} = \hat{\mathbf{z}}$ and two compatible printer poses for all other cases. A geometrical rule is established to further constrain the problem such that C is uniquely defined:

$$C \leftarrow -sign(\hat{n}_y)(-90 + acos(\hat{\mathbf{x}} \cdot \hat{\mathbf{n}})).$$

This dictates that the B-axis local x-component always points to the positive global x-direction. The B-angle is now fully defined as:

$$B \leftarrow -sign(\hat{n}_y)(-90 + acos(\hat{\mathbf{n}} \cdot [n_x, n_y, 0])).$$

One problem remains with this formulation: The C-angle becomes unstable whenever $n_y \sim 0$ (i.e., C instantly changes signs when $\hat{n}_y$ changes from mildly negative to mildly positive). To prevent this instability, we establish an additional rule: flip the C (and B) sign whenever an instantaneous angle change larger than 40 degrees is detected, effectively annulling it. This sign change carries over until the interconnect trace is completed or another sudden sign change is detected. Lastly, defining the corresponding X, Y, Z positions is a straightforward geometrical problem.

Supplemental Tables

Table S1: Comparison of on-tissue fabrication techniques of conductive layers.

	Microjet [This work]	**Aerosol**[33]	**Extrusion**[20,34–37]	**Drawn-on-skin**[38–40]
Tracing method	5-axis robot	3-axis robot	3- or 6-axis robot	Stencil
Target surface	Hairy scalp, 3D curvature	Hairless, Near flat	Hairless, Near flat	Hairless, Near flat
Ink type	PEDOT:PSS	Ag	Ag, C, EGaIn	Ag-PEDOT:PSS, P3HT-NF
Minimum feature size	2mm	10 µm	5 µm	300 µm
Spanned area[a]	$\sim$ 300$\times$300 mm	$\sim$ 10$\times$30 mm	39$\times$74 mm	$\sim$150$\times$150 mm
Sensor	EEG	Interconnect	Strain sensor, Interconnect	EMG, ECG, TENS, Transistor

[a]Estimated from figures when not reported explicitly.

Table S2: Comparison of the dried ink properties from various ink formulas

Ink Formulas[a]	**Conductivity (S/cm)**	**Young's modulus (MPa)**	**Elongation at break (mm/mm)**
No additive	< 1	2000	0.01
+ 1x DMSO	20	2000	0.01
+ 3x DMSO	170	1500	0.1
+ 5x DMSO	144	875	0.09
+ 1x glycerol	7.23	130	0.46
+ 0.193x NaCl + 1x glycerol[b]	**2.9**	**28**	**0.56**
+ 2x DMSO + 1x glycerol[c]	**83**	**66**	**0.3**
+ 2x glycerol	25.6	fragile	fragile

[a]The baseline formula (no additive) consists of 60 mg dried PEDOT:PSS added to 2 g DI water. For the rest, additives were added according to their mass relative to dry PEDOT:PSS. [b]Selected electrode ink recipe.[c]Selected interconnect ink recipe.

Table S3: Types of ink dispensing tools and specifications.[12,14,41]

	Microjet[a] [This work]	**Inkjet**	**Aerosol**	**Extrusion**
Actuation mechanism	Collision-type plunger	Bend-type actuator or thermo bubble	Atomization and gas flow	Pneumatic, piston or screw-type
Maximum ink viscosity	10^6 mPa.s	50 mPa.s	1000 mPa.s	$> 3\times10^5$ mPa.s
Type	Drop-on-demand $>$ 0.5nL	Drop-on-demand$\sim$1pL or continuous jet	Continuous stream of droplets	Continuous stream
Maximum jet frequency	150-3000 Hz	$>$20 kHz	Not applicable	Not applicable
Print resolution	100 µm	20 µm	10-50 µm	2-30 µm
Nozzle standoff	Non-contact (0.5-10 mm)	Non-contact (1mm)	Non-contact (1-5 mm)	Contact ($<$ 1 mm)

[a]Microjet is also a type of inkjet (both are drop-on-demand type jetting); however, it is often assigned a separate terminology due to their significantly distinct specifications.

Table S4: Comparison of various electrode types under different parameters

Electrode type	References	Signal quality	Lifetime	Hair compatibility	Thinness	Comfort
		Specific impedance (without abrasion) < 50 kΩ.cm^2: Good[16] 50-200kΩ.cm^2: Medium > 200 kΩ.cm^2: Poor	> 24h: Good 5-24h: Medium < 5h: Poor	Hair length > 2cm: Good < 2cm: Medium Shaved: Poor	< 0.1mm: Good 0.1-1mm: Medium > 1mm: Poor	[a]Pressure points [b]Cause itchiness
Dry (pressure)	[42–44]	Poor	Good	Good	Poor	Poor[a]
Wet gel	[18,42,45,46]	Good	Poor	Good	Poor	Poor[b]
Dry (e-tattoo)	[45–47]	Medium	Good	Poor	Good	Good
On-scalp printed	This work	Good	Medium	Medium	Good	Good

Supplemental Figures

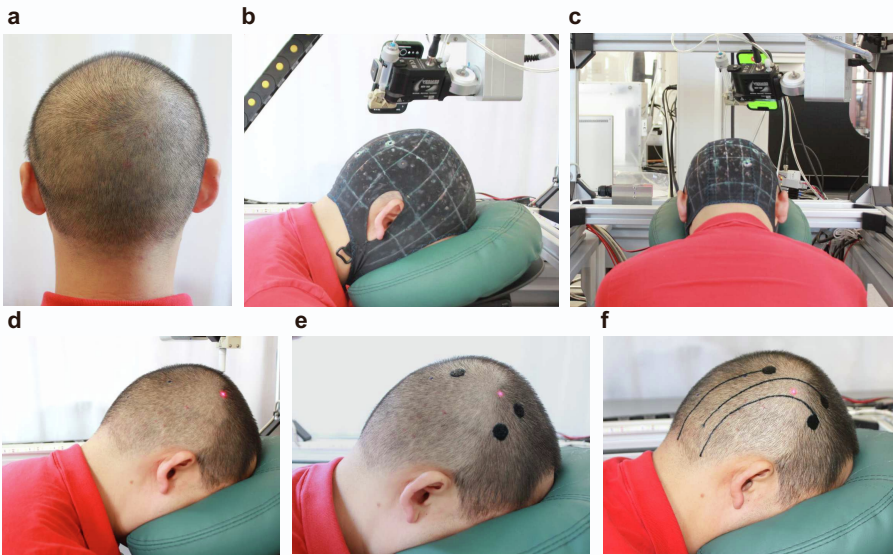

Figure. S1: Main steps of the printing process. (a) Subject with short hair. (b) Side and (c) back views from the subject wearing a fitted cap with the head resting on a massage chair inside the robot system. A camera attached to the printer's end effector circles 360 degrees to generate a 3D model of the skull shape. (d) A soft prong attached to the end-effector (white adaptor in the background) probes the 3D coordinates of three fiducial points on the head to pose match the digital 3D model. (e) Electrodes printed using the low interface impedance ink. (f) Interconnects printed using the high interface impedance but low bulk resistance ink.

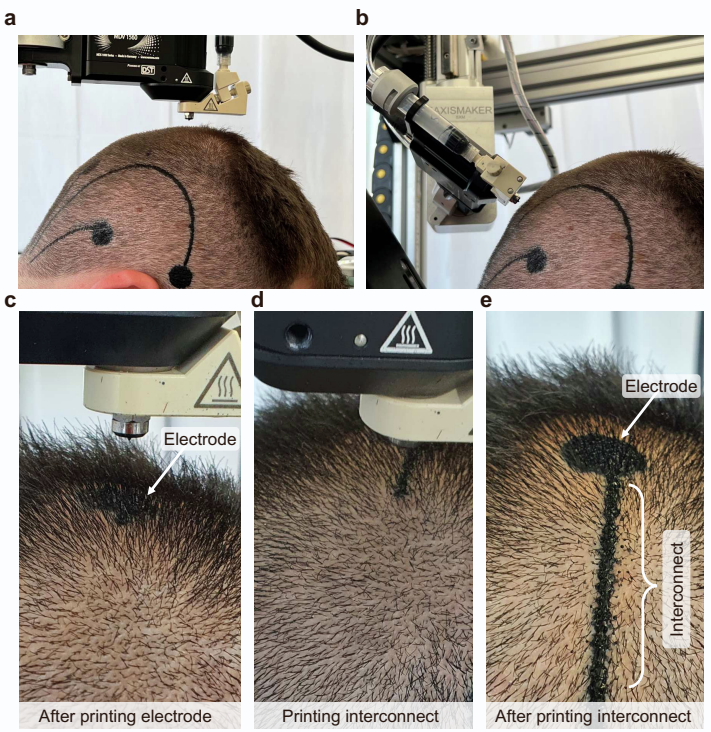

Figure. S2: On-scalp microjetting process. (a-b) 5-axis movement for conformal printing over large curvatures. (c-e) close view of the print at different states: after printing the electrode, during the printing of the interconnect, and after printing the interconnect.

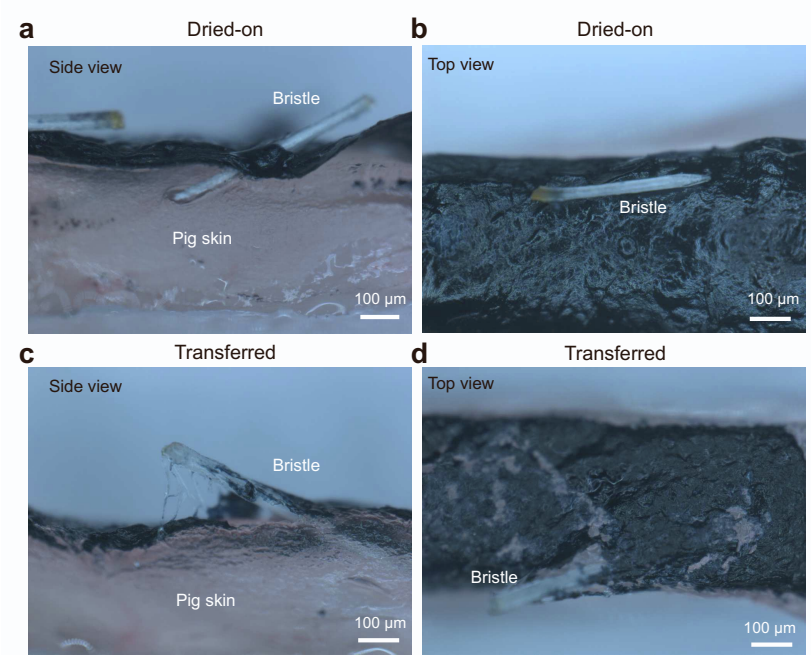

Figure. S3: Hair incompatibility of the transfer method. (a,b) The ink cured directly on the pig skin with hair bristle forms a continuous and conformal film. (c,d) The ink dried on a carrier substrate and subsequently transferred to the pig skin is lifted by the hair bristle and cracks in multiple locations.

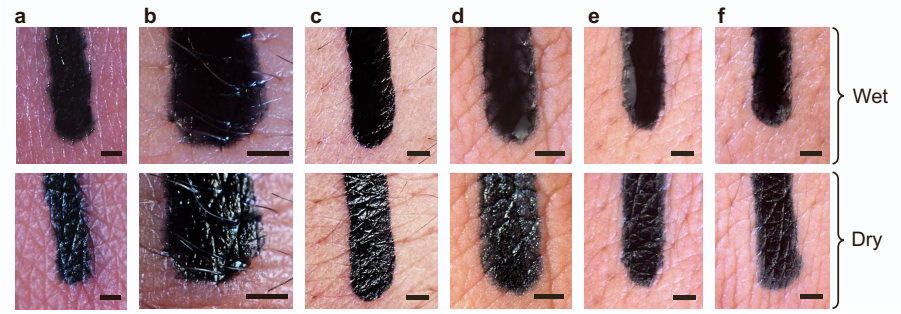

Figure. S4: Images of multiple printed films on human skin in wet and dry states, showing repeatable conformal topography across various human skin textures. (Scale bar: 1mm)

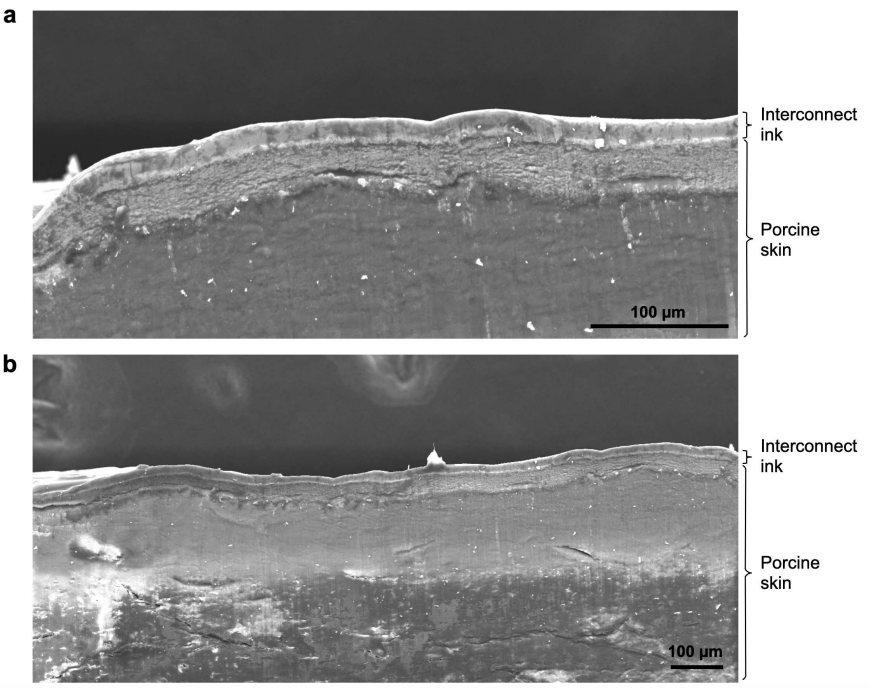

Figure. S5: Cross-section images of the interconnect ink printed on porcine skin showing conformal topography.

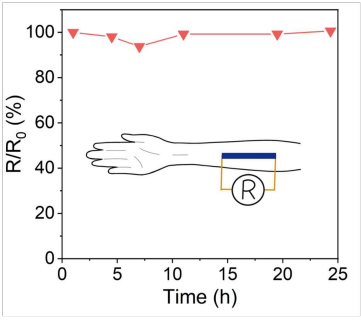

Figure. S6: The resistance of the interconnect trace printed on the human forearm for over 24 hours.

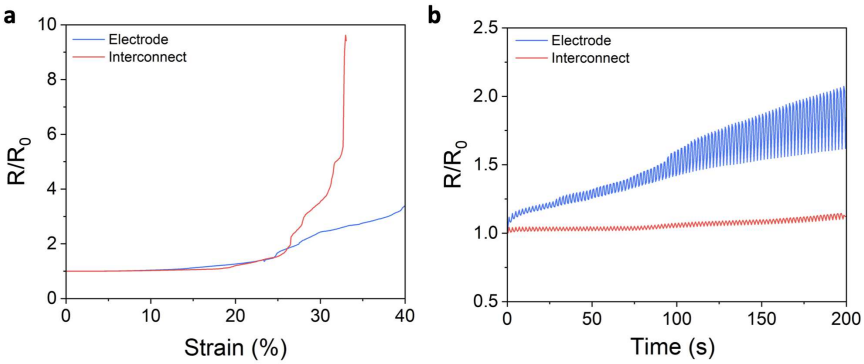

Figure. S7: Electrical stability of free-standing electrode and interconnect films under repeated stretching. (a) Relative resistance variation of electrode and interconnect films under tensile strain. Both are stable under 25% strain which is well within the scalp strain to failure.[48] (b) The resistance change of the electrode and interconnect films under repeated stretching-releasing at 10% strain for 100 cycles. Note that the electrode resistance is inconsequential to the on-scalp printed EEG system (negligible compared to the interconnect) due to its large area and small length. The interconnect film resistance is approximately stable ($<$20% increase).

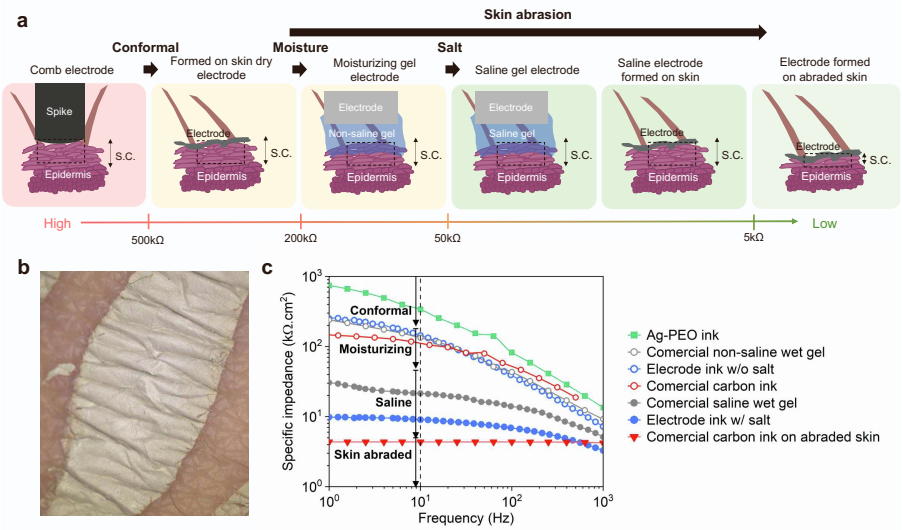

Figure. S8: Effects of conformal contact, ink additives and skin conditioning on the electrode-skin interface impedance. (a) Schematic showing different electrode types and the corresponding impedance range. (b) Optical image of an Ag-PEO ethanol- and water-based film cured on the skin. (c) Specific electrode-skin impedance for different commercial and custom-made electrodes showing the cumulative effects of conformal contact, hydration, salt additives, and skin abrasion. The impedance of the Ag-PEO film formed on the skin ($200 \sim 300$ kΩ) is lower than comb-type electrodes (> 500 kΩ)[19] thanks to its conformal contact. Films and gels that moisturize the skin and increase the salt concentration further decrease the impedance to levels under 200 $k\Omega$ and 50 $k\Omega$, respectively. When the skin is abraded, the impedance is low regardless of moisturizing and salt concentration effects. For example, following abrasion, a commercial carbon ink impedance is lowered from > 100kΩ to < 5kΩ.

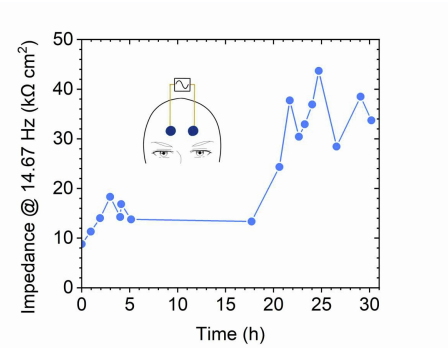

Figure. S9: The impedance of dried electrode ink on the forehead over time when the EIS frequency is 14.67 Hz. The impedance showed some fluctuation and slowly increased over time, possibly because of the varying skin hydration states over the course of time and the loss of residual water in the electrode, which can affect ion mobility.

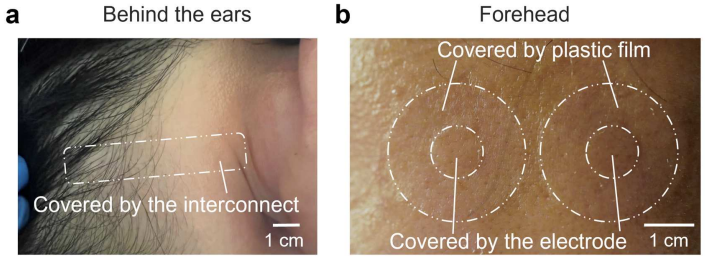

Figure. S10: Photos of the skin following the removal of inks after 24h of exposure showing no signs of allergic reactions. (a) Interconnect and (b) electrode inks.

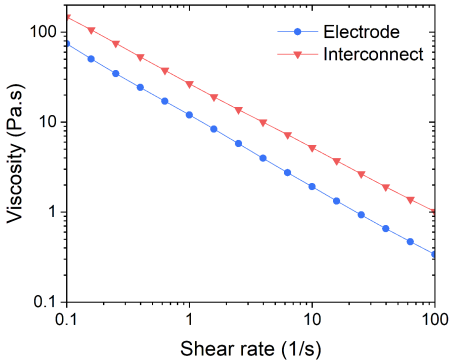

Figure. S11: Viscosity measurements showing shear thinning behavior of the interconnect and electrode inks.

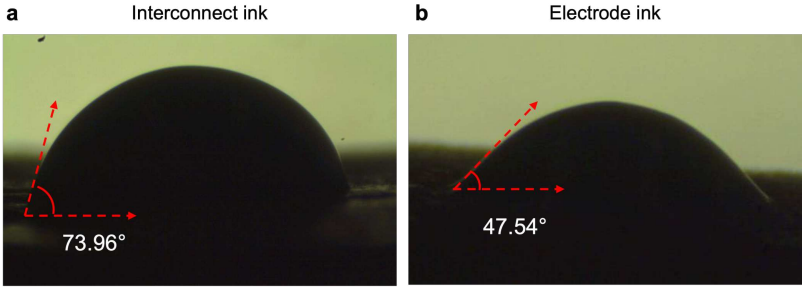

Figure. S12: Contact angle measurements on pig skin. (a) Interconnect ink and (b) electrode ink.

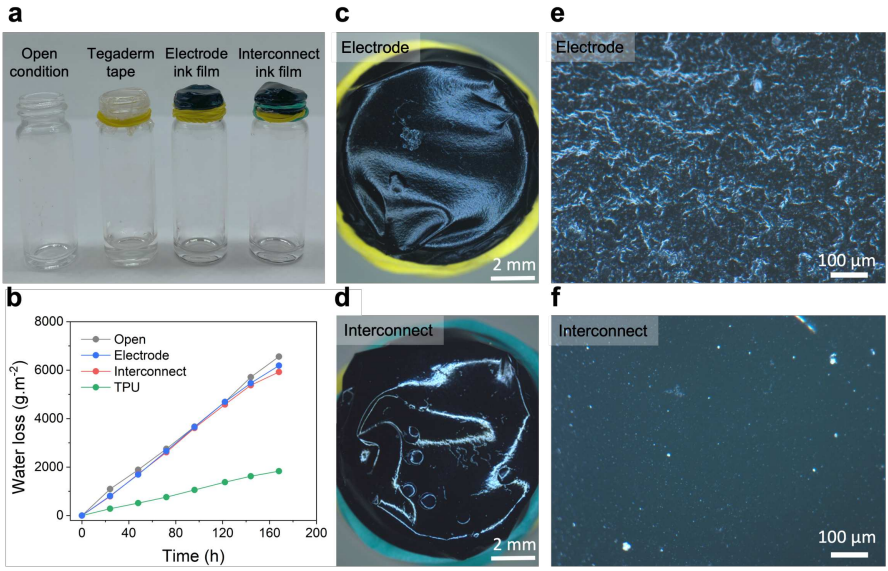

Figure. S13: Water Vapor Transmission Rate (WVTR) measurements to evaluate the breathability of different films. (a) The weight of water-filled vials was recorded over 7 days for different cover conditions: open, covered with Tegaderm (47 µm), and covered with interconnect and electrode ink films ($\sim$ 30 µm). The interconnect and electrode WVTRs were similar to that of an open vial, indicating excellent breathability, far superior to the commonly used Tegaderm film. Optical microscopy inspection of the (c,e) electrode and (d,f) interconnect films shows a continuous surface without cracks or visible pores, indicating that the high WVTR is intrinsic to the material.

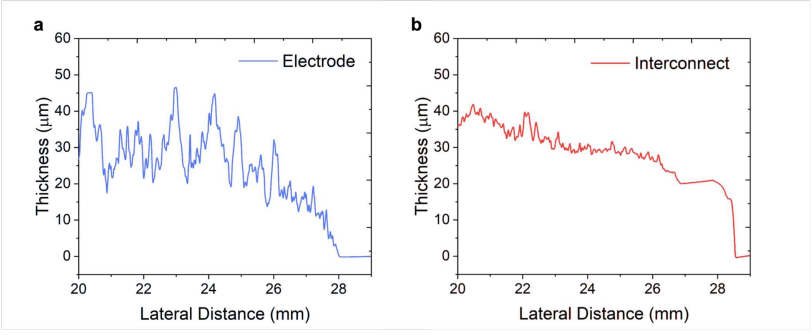

Figure. S14: Atomic force microscopy measurements of the electrode and interconnect films printed on PDMS after drying using the same printing settings (jetting parameters and translation speed) used for on-body printing.

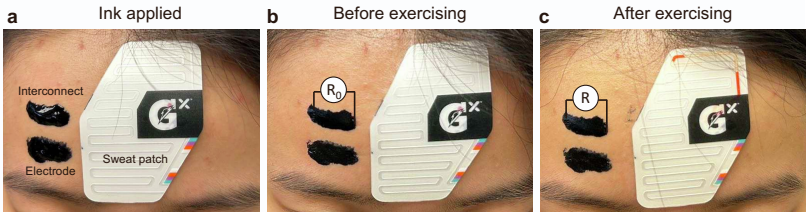

Figure. S15: Photos of the ink sweat stability test, showing the ink trace and sweat pad on the subject's forehead.

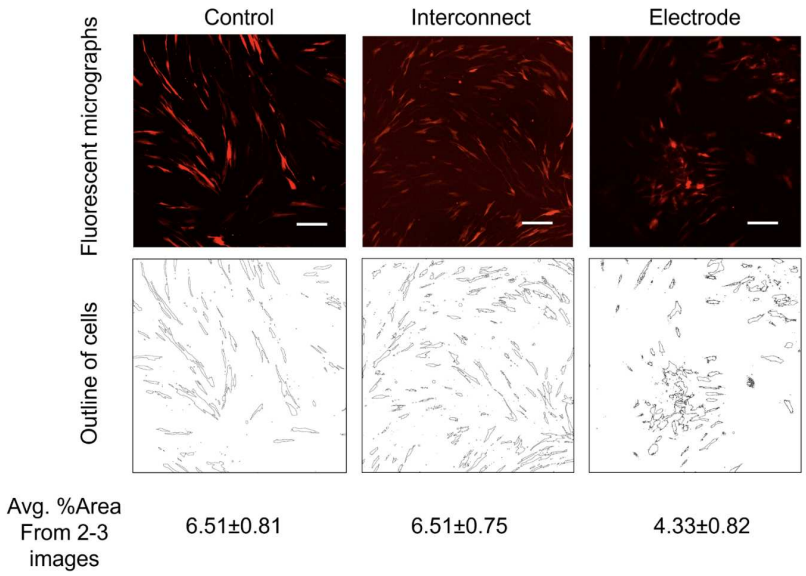

Figure. S16: Quantitative analysis of the human skin fibroblast cells. Representative fluorescent micrographs on day 3 of the cells cultured on different substrates (first row), where the cells directly cultured on a 12-well plate without adding any ink materials were used as a control and the corresponding binarized images should the cell outlines (second row) to compute the percentage area of the cells compared to the entire field of view. The average cell area percentage from 2∼3 images for each is shown on the bottom row. Since in all the experiments, the cell seeding density and the field of view are the same, the percentage area can be used to reflect biocompatibility on various substrates. The results show that the interconnect has similar biocompatibility to the control while the electrode shows slightly lower biocompatibility than the control. Scale: 10 μm.

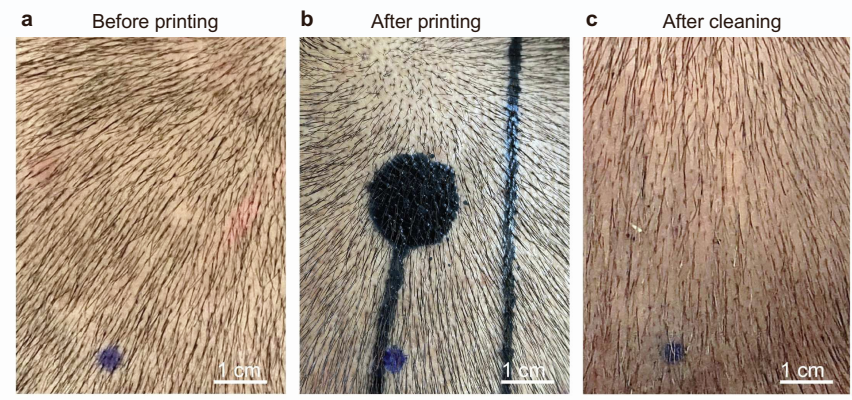

Figure. S17: Close-up photos of the scalp after printing. (a) Before printing, (b) after printing, and (c) after the cleaning of the electrode and interconnect traces post 6h of wear. A purple dot is used as a fixed reference across the photos. No skin irritation is observed.

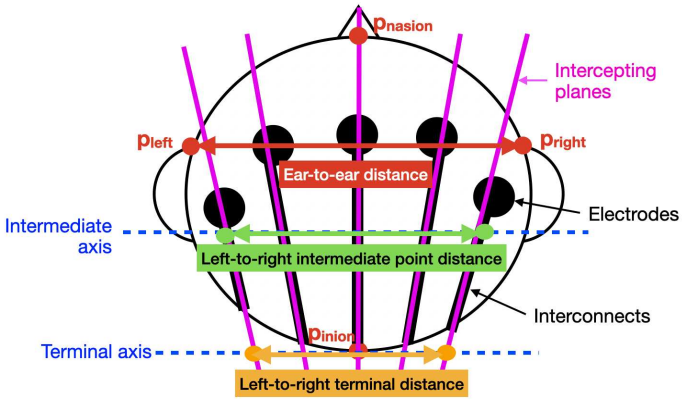

Figure. S18: Top view schematic of the head illustrating how intermediate reference points spanning 80% the ear-to-ear distance and terminal points spanning 75% the ear-to-ear distance define the intercepting planes used by the algorithm for interconnect routing.

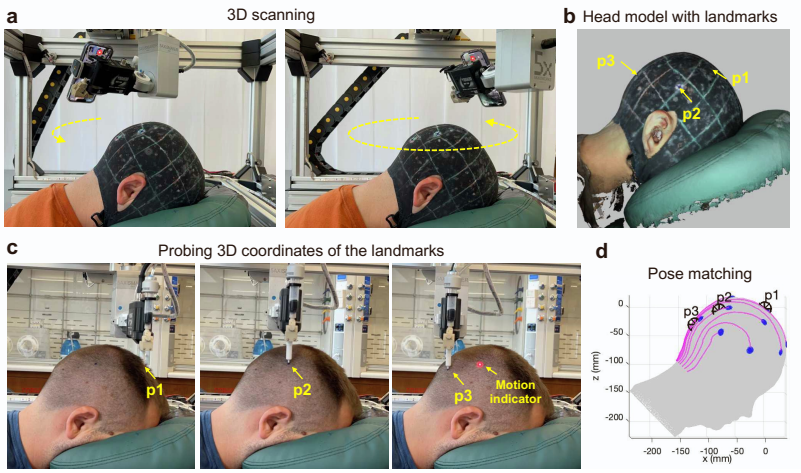

Figure. S19: Printer pose correction procedure. (a) Three holes on the 3D-scanned elastic cap are used to paint three dots on the subject head to serve as landmarks. (b) The landmarks appear on the 3D head model (p1,p2,p3), where the electrode and interconnect layout will be generated. (c) When the subject sits down for printing to be initiated, the coordinates of the three landmarks are probed in the printer's coordinate system using a spring-loaded prong (white piece attached to the nozzle tip). (d) The toolpath is corrected for the user's pose by matching the digital landmark coordinates (black asterisk) to the physical landmark coordinates (black circles), and the printing can be initiated.

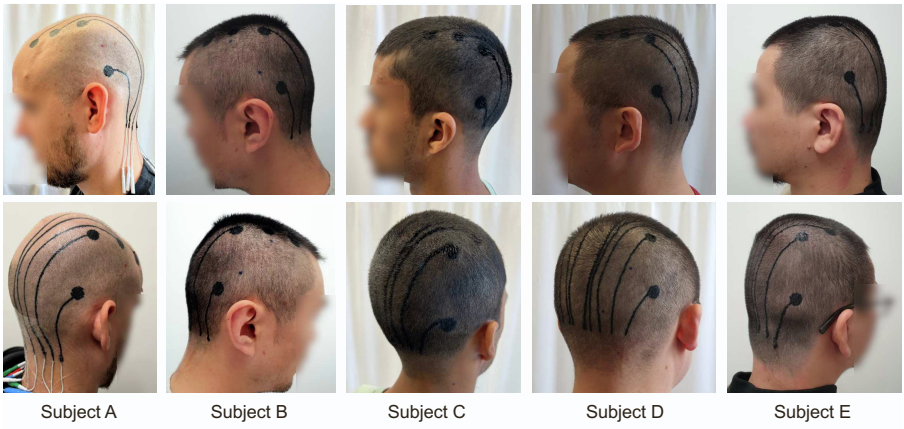

Figure. S20: Photographs of the 5 human subjects that participated in this study with the on-scalp printed EEG electrodes and interconnects.

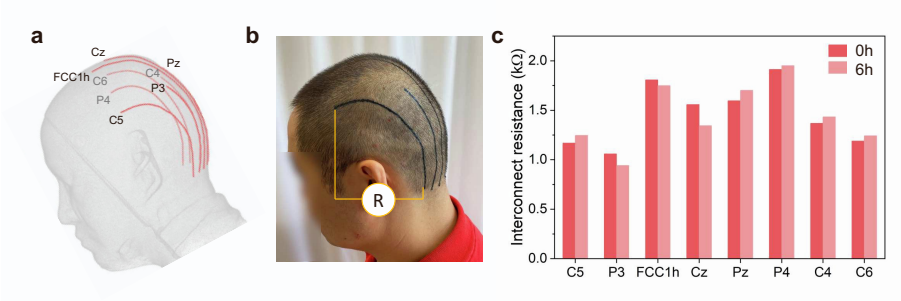

Figure. S21: End-to-end interconnect resistance measurement on the scalp. (a) The montage (8 interconnects) used. (b) Side view photo of the printed interconnects. (c) The average interconnect resistance ranges from $1\sim 2k\Omega$, which is roughly a tenth of the typical electrode contact impedance (Figure 4). This confirms that the interconnect ink conductivity is sufficiently high such that the interconnect will not compromise the amplifier noise-rejection ability. The interconnect resistance was stable for the measurement duration (6h) indicating all traces were mechanically robust and maintained their physical integrity.

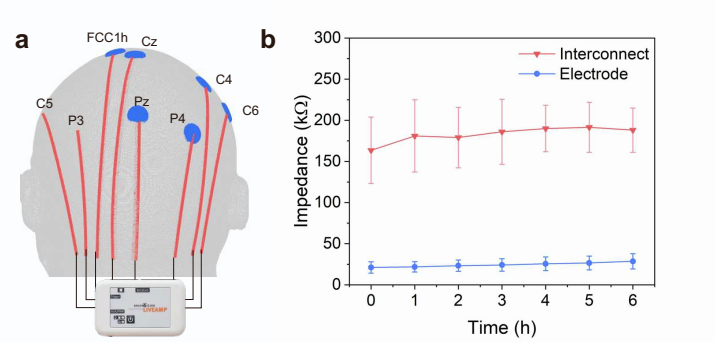

Figure. S22: Comparison between the overall interconnect and electrode contact impedance measured simultaneously with the EEG DAQ. (a) Montage used for the measurement (two channels with interconnects only and six channels of interconnects with electrodes). (b) Average (symbol) and standard deviation (error bar) over the course of 6h from the time of printing. The average impedance of the channels with electrodes is small relative to that of the channels with only interconnect (Figure 4). This shows that the low contact impedance of the electrode ink and the high contact impedance of the interconnect ink make the electrode the dominant circuit to the skin, which should enforce brain signal pickup from the electrode site. The electrode-interconnect impedance ratio is stable over time.

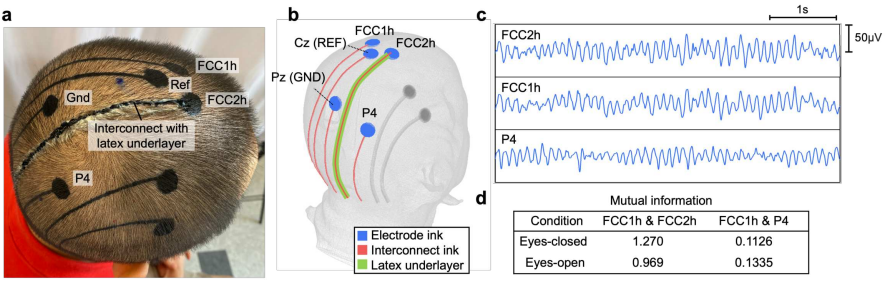

Figure. S23: Interconnect ink electrical insulation validation against that of an interconnect with a liquid latex substrate. (a) Photo and (b) schematic of the experiment. Two measuring electrodes were placed close together along the boundary between central and pariental lobes - FCC1h using the bare interconnect ink and FCC2h using the interconnect ink over a thick layer of electrically insulating liquid latex film (green in the schematic). A third measuring electrode was placed on the back of the head (P4). The reference and ground electrodes were placed at Cz and Pz, respectively. (c) Representative EEG recordings measured with the subject at rest by the three measuring electrodes. The signals recorded by the channels using the extra interconnect insulation (FCC2h) and the bare interconnect ink (FCC1h) are very similar, suggesting that the signal acquisition is mostly unchanged by the additional insulating layer. In the meantime, the amplitude of the P4 signal is markedly distinct. (d) Mutual information (MI) during 60 s of eyes open and closed. The high FCC1h&FCC2h MI values mean that the signal measured with additional latex insulation (FCC2h) and bare interconnect (FCC1h) have high synchronization or shared information, while FCC1h&P4 low values mean high independence. This demonstrates the effectiveness of the interconnect ink in acting as natural insulation, avoiding significant pick-up of brain signals along the interconnect path at the back of the head.

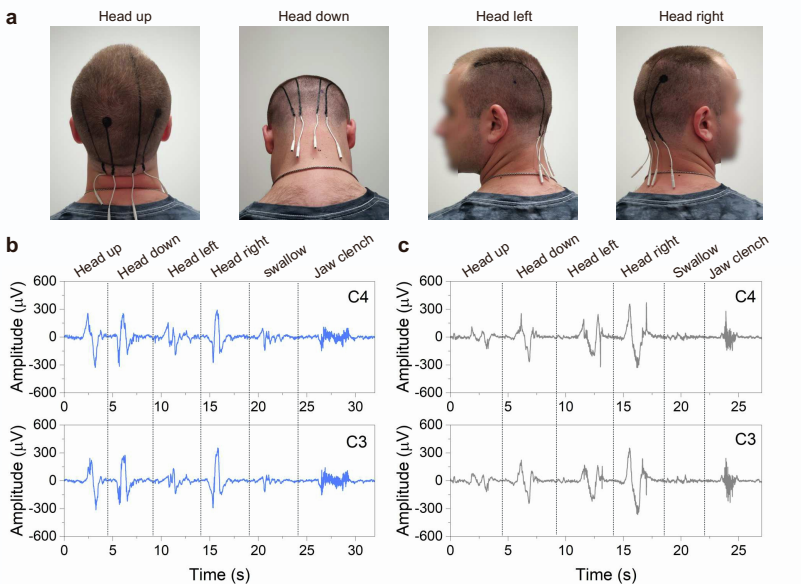

Figure. S24: Motion artifact test. (a) Head positions during the test. EEG signals for (b) the printed system and (c) a conventional EEG cap with gel electrodes (Figure 1j, left). The curves indicate equivalent sensitivity to movement.

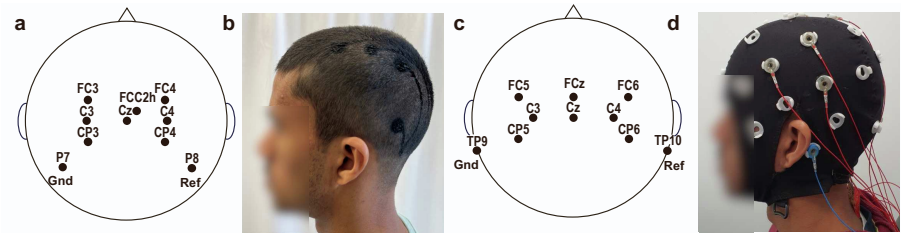

Figure. S25: Montages used in the BCI tests. (a,b) On-scalp printed electrodes and (c,d) gel electrodes.

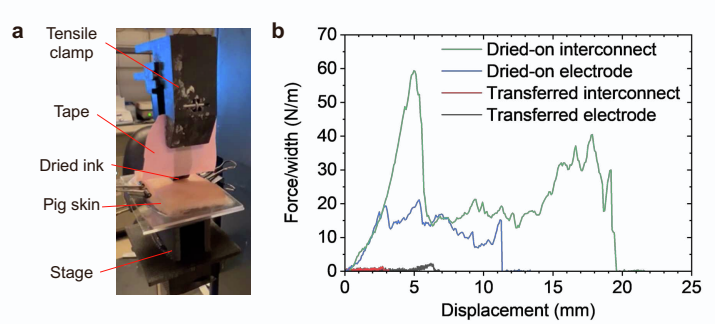

Figure. S26: Comparison of the adhesion force between dried-on e-tattoo and transferred e-tattoo. (a) Peel test setup. The tape is for peeling one end of the dried ink off the pig skin. The pig skin is glued to a glass slide clamped on the custom 3D-printed sample stage. The sample stage is designed to connect to the metal connector of the tensile tester. (b) Normalized peeling force versus peeling distance. The peeling force is normalized by the width of the ink strip.

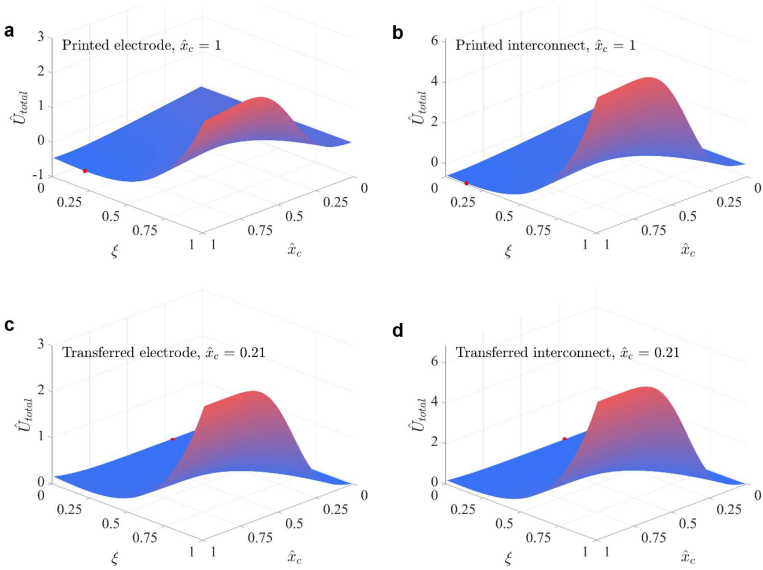

Figure. S27: Normalized total energy landscape analysis of electrode and interconnect films conformability with the skin using different fabrication procedures. (a) Dried-on electrode, (b) dried-on interconnect, (c) transferred electrode, and (d) transferred interconnect. Red dots indicate global energy minima. $\hat{x}_c = 1$ represents fully conformed, $0 < \hat{x}_c < 1$ means partially conformed, and $\hat{x}_c = 0$ denotes non-conformed.

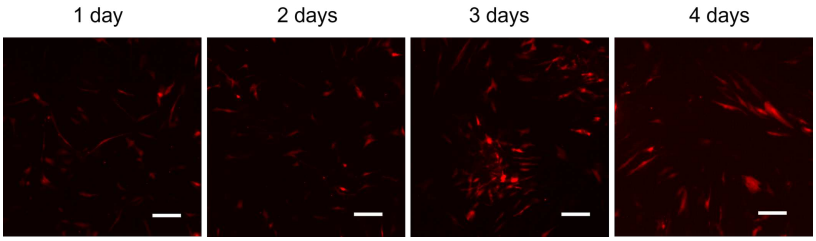

Figure. S28: Microscope images of human skin fibroblasts cultured on the electrode films as substrates. Scale: 10 μm.

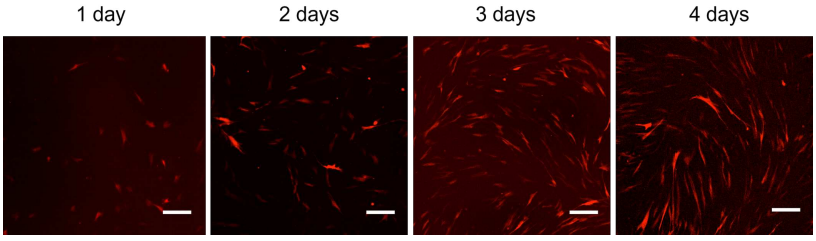

Figure. S29: Microscope images of human skin fibroblasts cultured on the interconnect films as substrates. Scale: 10 μm.

References

1. Zack, M.M. (2017): National and state estimates of the numbers of adults and children with active epilepsy—united states, 2015. MMWR Morb. Mortal. Wkly Rep. **66**. https://doi.org/10.15585/mmwr.mm6631a1
2. England, M.J., Liverman, C.T., Schultz, A.M., Strawbridge, L.M. (2012): Epilepsy across the spectrum: Promoting health and understanding.: A summary of the institute of medicine report. Epilepsy & Behav. **25**(2), 266–276. https://doi.org/10.1016/j.yebeh.2012.06.016
3. Leijten, F.S., Consortium, D.T., van Andel, J., Ungureanu, C., Arends, J., Tan, F., van Dijk, J., Petkov, G., Kalitzin, S., Gutter, T., *et al.*(2018): Multimodal seizure detection: A review. Epilepsia **59**, 42–47. https://doi.org/10.1111/epi.14047
4. Elger, C.E., Hoppe, C. (2018): Diagnostic challenges in epilepsy: seizure under-reporting and seizure detection. Lancet Neurol. **17**(3), 279–288. https://doi.org/10.1016/S1474-4422(18)30038-3
5. Benbadis, S.R. (2015): What type of EEG (or EEG-video) does your patient need? Expert Rev. Neurother. **15**(5), 461–464. https://doi.org/10.1586/14737175.2015.1029918
6. Askamp, J., van Putten, M.J. (2014): Mobile EEG in epilepsy. Int. J. Psychol. **91**(1), 30–35. https://doi.org/10.1016/j.ijpsycho.2013.09.002

7. Kennedy, J.D., Gerard, E.E. (2012): Continuous EEG monitoring in the intensive care unit. Curr. Neurol. Neurosci. Rep. **12**, 419–428. https://doi.org/10.1007/s11910-012-0289-0
8. Nobili, L., de Weerd, A., Rubboli, G., Beniczky, S., Derry, C., Eriksson, S., Halasz, P., Högl, B., Santamaria, J., Khatami, R., *et al.*(2021): Standard procedures for the diagnostic pathway of sleep-related epilepsies and comorbid sleep disorders: An ean, esrs and ilae-europe consensus review. Eur. J. Neurol. **28**(1), 15–32. https://doi.org/10.1111/ene.14468
9. Sinha, S.R., Sullivan, L.R., Sabau, D., Orta, D.S.J., Dombrowski, K.E., Halford, J.J., Hani, A.J., Drislane, F.W., Stecker, M.M. (2016): American clinical neurophysiology society guideline 1: minimum technical requirements for performing clinical electroencephalography. Neurodiagn. J. **56**(4), 235–244. https://doi.org/10.1080/21646821.2016.1245527
10. Slifer, K.J., Avis, K.T., Frutchey, R.A. (2008): Behavioral intervention to increase compliance with electroencephalographic procedures in children with developmental disabilities. Epilepsy & Behav. **13**(1), 189–195. https://doi.org/10.1016/j.yebeh.2008.01.013
11. Bruno, E., Viana, P.F., Sperling, M.R., Richardson, M.P. (2020): Seizure detection at home: Do devices on the market match the needs of people living with epilepsy and their caregivers? Epilepsia **61**, 11–24. https://doi.org/10.1111/epi.16521
12. Li, H., Liu, J., Li, K., Liu, Y. (2019): Piezoelectric micro-jet devices: A review. Sens. Actuators A Phys. **297**, 111552. https://doi.org/10.1016/j.sna.2019.111552
13. Abbas, A., Bajwa, I. (2017): Inkjet printing of ag nanoparticles using dimatix inkjet printer, no 1. Protoc. Rep. https://doi.org/10.13140/RG.2.2.17084.64646
14. Godlinski, D., Zichner, R., Zöllmer, V., Baumann, R.R. (2017): Printing technologies for the manufacturing of passive microwave components: antennas. IET Microw. Antennas Propag. **11**(14), 2010–2015. https://doi.org/10.1049/iet-map.2017.0042
15. Hutchings, I.M., Martin, G.D.: Inkjet Technology for Digital Fabrication. John Wiley & Sons, Inc., United Kingdom (2012). https://doi.org/10.1002/9781118452943
16. Ferree, T.C., Luu, P., Russell, G.S., Tucker, D.M. (2001): Scalp electrode impedance, infection risk, and EEG data quality. Clin. Neurophysiol. **112**(3), 536–544. https://doi.org/10.1016/S1388-2457(00)00533-2
17. Tam, H., Webster, J.G. (1977): Minimizing electrode motion artifact by skin abrasion. IEEE Trans. Biomed. Eng. (2), 134–139. https://doi.org/10.1109/TBME.1977.326117
18. Kappenman, E.S., Luck, S.J. (2010): The effects of electrode impedance on data quality and statistical significance in erp recordings. Psychophysiol. **47**(5), 888–904. https://doi.org/10.1111/j.1469-8986.2010.01009.x
19. Chi, Y.M., Jung, T.-P., Cauwenberghs, G. (2010): Dry-contact and noncontact biopotential electrodes: Methodological review. IEEE Rev.

Biomed. Eng. **3**, 106–119. https://doi.org/10.1109/RBME.2010.2084078
20. Zhu, Z., Guo, S.-Z., Hirdler, T., Eide, C., Fan, X., Tolar, J., McAlpine, M.C. (2018): 3D printed functional and biological materials on moving freeform surfaces. Adv. Mater. **30**(23), 1707495. https://doi.org/10.1002/adma.201707495
21. Clar, E., Her, C., Sturelle, C. (1975): Skin impedance and moisturization. J. Soc. Cosmet. Chem. **26**, 337–353
22. Tregear, R. (1965): Interpretation of skin impedance measurements. Nature **205**(4971), 600–601. https://doi.org/10.1038/205600a0
23. Geddes, L.A. (1972): Electrodes and the measurement of bioelectrical events. WILEY-INTERSCIENCE, 99–102. https://doi.org/10.1086/407587
24. Yamamoto, T., Yamamoto, Y. (1976): Electrical properties of the epidermal stratum corneum. Med. Biol. Eng. **14**, 151–158. https://doi.org/10.1007/BF02478741
25. Rosell, J., Colominas, J., Riu, P., Pallas-Areny, R., Webster, J.G. (1988): Skin impedance from 1 hz to 1 mhz. IEEE Trans. Biomed. Eng. **35**(8), 649–651. https://doi.org/10.1109/10.4599
26. Li, G., Wang, S., Duan, Y.Y. (2017): Towards gel-free electrodes: A systematic study of electrode-skin impedance. Sens. Actuators B Chem. **241**, 1244–1255. https://doi.org/10.1016/j.snb.2016.10.005
27. Liu, S., Rao, Y., Jang, H., Tan, P., Lu, N. (2022): Strategies for body-conformable electronics. Matter **5**(4), 1104–1136. https://doi.org/10.1016/j.matt.2022.02.006
28. Wang, L., Lu, N. (2016): Conformability of a Thin Elastic Membrane Laminated on a Soft Substrate With Slightly Wavy Surface. J. Appl. Mech. **83**(4), 041007. https://doi.org/10.1115/1.4032466
29. Gallego Martínez, E.E., González Mitjans, A., Garea-Llano, E., Bringas-Vega, M.L., Valdes-Sosa, P.A. (2021): Automatic detection of fiducial landmarks toward the development of an application for digitizing the locations of EEG electrodes: Occipital structure sensor-based work. Front. Neurosci. **15**, 526257. https://doi.org/10.3389/fnins.2021.526257
30. Giacometti, P., Perdue, K.L., Diamond, S.G. (2014): Algorithm to find high density EEG scalp coordinates and analysis of their correspondence to structural and functional regions of the brain. J. Neurosci. Methods **229**, 84–96. https://doi.org/10.1016/j.jneumeth.2014.04.020
31. Jasper, H. (1958): Report of the committee on methods of clinical examination in electroencephalography. Electroencephalogr. Clin. Neurophysiol. **10**, 370–375. https://doi.org/10.1016/0013-4694(58)90053-1
32. Oostenveld, R., Praamstra, P. (2001): The five percent electrode system for high-resolution EEG and ERP measurements. Clin. Neurophysiol. **112**(4), 713–719. https://doi.org/10.1016/S1388-2457(00)00527-7
33. Williams, N.X., Noyce, S., Cardenas, J.A., Catenacci, M., Wiley, B.J., Franklin, A.D. (2019): Silver nanowire inks for direct-write electronic tattoo applications. Nanoscale **11**(30), 14294–14302. https://doi.org/10.

1039/C9NR03378E
34. Choi, Y., Ryu, N., Kim, M.J., Dementyev, A., Bianchi, A.: Bodyprinter: Fabricating circuits directly on the skin at arbitrary locations using a wearable compact plotter. In: Proceedings of the 33rd Annual ACM Symposium on User Interface Software and Technology, pp. 554–564 (2020). https://doi.org/10.1145/3379337.3415840
35. Zhu, Z., Park, H.S., McAlpine, M.C. (2020): 3D printed deformable sensors. Science Adv. **6**(25), 5575. https://doi.org/10.1126/sciadv.aba5575
36. Kwon, Y.W., Ahn, D.B., Park, Y.-G., Kim, E., Lee, D.H., Kim, S.-W., Lee, K.-H., Kim, W.-Y., Hong, Y.-M., Koh, C.S., *et al.*(2024): Power-integrated, wireless neural recording systems on the cranium using a direct printing method for deep-brain analysis. Science Advances **10**(14), 3784. https://doi.org/10.1126/sciadv.adn3784
37. Park, Y.-G., Kwon, Y.W., Koh, C.S., Kim, E., Lee, D.H., Kim, S., Mun, J., Hong, Y.-M., Lee, S., Kim, J.-Y., *et al.*(2024): In-vivo integration of soft neural probes through high-resolution printing of liquid electronics on the cranium. Nature communications **15**(1), 1772. https://doi.org/10.1038/s41467-024-45768-0
38. Zhang, L., Ji, H., Huang, H., Yi, N., Shi, X., Xie, S., Li, Y., Ye, Z., Feng, P., Lin, T., *et al.*(2020): Wearable circuits sintered at room temperature directly on the skin surface for health monitoring. ACS Appl. Mater. Interfaces **12**(40), 45504–45515. https://doi.org/10.1021/acsami.0c11479
39. Ershad, F., Thukral, A., Yue, J., Comeaux, P., Lu, Y., Shim, H., Sim, K., Kim, N.-I., Rao, Z., Guevara, R., *et al.*(2020): Ultra-conformal drawn-on-skin electronics for multifunctional motion artifact-free sensing and point-of-care treatment. Nat. Commun. **11**(1), 3823. https://doi.org/10.1038/s41467-020-17619-1
40. Ershad, F., Houston, M., Patel, S., Contreras, L., Koirala, B., Lu, Y., Rao, Z., Liu, Y., Dias, N., Haces-Garcia, A., *et al.*(2023): Customizable, reconfigurable, and anatomically coordinated large-area, high-density electromyography from drawn-on-skin electrode arrays. PNAS Nexus **2**(1), 291. https://doi.org/10.1093/pnasnexus/pgac291
41. Tong, C.: Advanced Materials for Printed Flexible Electronics. Springer, United States of America (2022). https://doi.org/10.1007/978-3-030-79804-8
42. Liao, L.-D., Wang, I.-J., Chen, S.-F., Chang, J.-Y., Lin, C.-T. (2011): Design, fabrication and experimental validation of a novel dry-contact sensor for measuring electroencephalography signals without skin preparation. Sensors **11**(6), 5819–5834. https://doi.org/10.3390/s110605819
43. Fiedler, P., Mühle, R., Griebel, S., Pedrosa, P., Fonseca, C., Vaz, F., Zanow, F., Haueisen, J. (2018): Contact pressure and flexibility of multi-pin dry EEG electrodes. IEEE Trans. Neural Syst. Rehabil. Eng. **26**(4), 750–757. https://doi.org/10.1109/TNSRE.2018.2811752

44. Chen, Y.-H., De Beeck, M.O., Vanderheyden, L., Carrette, E., Mihajlović, V., Vanstreels, K., Grundlehner, B., Gadeyne, S., Boon, P., Van Hoof, C. (2014): Soft, comfortable polymer dry electrodes for high quality ECG and EEG recording. Sensors **14**(12), 23758–23780. https://doi.org/10.3390/s141223758
45. Reis Carneiro, M., Majidi, C., Tavakoli, M. (2022): Multi-electrode printed bioelectronic patches for long-term electrophysiological monitoring. Adv. Funct. Mat. **32**(43), 2205956. https://doi.org/10.1002/adfm.202205956
46. Ferrari, L.M., Ismailov, U., Badier, J.-M., Greco, F., Ismailova, E. (2020): Conducting polymer tattoo electrodes in clinical electro-and magneto-encephalography. npj Flexible Electron. **4**(1), 4. https://doi.org/10.1038/s41528-020-0067-z
47. Shin, J.H., Kwon, J., Kim, J.U., Ryu, H., Ok, J., Joon Kwon, S., Park, H., Kim, T.-i. (2022): Wearable EEG electronics for a brain-AI closed-loop system to enhance autonomous machine decision-making. npj Flexible Electron. **6**(1), 32. https://doi.org/10.1038/s41528-022-00164-w
48. Falland-Cheung, L., Scholze, M., Lozano, P.F., Ondruschka, B., Tong, D.C., Brunton, P.A., Waddell, J.N., Hammer, N. (2018): Mechanical properties of the human scalp in tension. Journal of the mechanical behavior of biomedical materials **84**, 188–197. https://doi.org/10.1016/j.jmbbm.2018.05.024